

ORIGINAL PAPER

Open Access



# The role of the antigorite + brucite to olivine reaction in subducted serpentinites (Zermatt, Switzerland)

Elias D. Kempf<sup>1\*</sup> , Jörg Hermann<sup>1</sup>, Eric Reusser<sup>2</sup>, Lukas P. Baumgartner<sup>3</sup> and Pierre Lanari<sup>1</sup>

## Abstract

Metamorphic olivine formed by the reaction of antigorite + brucite is widespread in serpentinites that crop out in glacier-polished outcrops at the Unterer Theodulglacier, Zermatt. Olivine overgrows a relic magnetite mesh texture formed during ocean floor serpentinization. Serpentinization is associated with rodingitisation of mafic dykes. Metamorphic olivine coexists with magnetite, shows high Mg# of 94–97 and low trace element contents. A notable exception is 4 µg/g Boron (> 10 times primitive mantle), introduced during seafloor alteration and retained in metamorphic olivine. Olivine incorporated 100–140 µg/g H<sub>2</sub>O in Si-vacancies, providing evidence for low SiO<sub>2</sub>-activity imposed by brucite during olivine growth. No signs for hydrogen loss or major and minor element diffusional equilibration are observed. The occurrence of olivine in patches within the serpentinite mimics the former heterogeneous distribution of brucite, whereas the network of olivine-bearing veins and shear zones document the pathways of the escaping fluid produced by the olivine forming reaction. Relic Cr-spinels have a high Cr# of 0.5 and the serpentinites display little or no clinopyroxene, indicating that they derive from hydrated harzburgitic mantle that underwent significant melt depletion. The enrichment of Mg and depletion of Si results in the formation of brucite during seafloor alteration, a pre-requisite for later subduction-related olivine formation and fluid liberation. The comparison of calculated bulk rock brucite contents in the Zermatt-Saas with average IODP serpentinites suggests a large variation in fluid release during olivine formation. Between 3.4 and 7.2 wt% H<sub>2</sub>O is released depending on the magnetite content in fully serpentinized harzburgites (average oceanic serpentinites). Thermodynamic modelling indicates that the fluid release in Zermatt occurred between 480 °C and 550 °C at 2–2.5 GPa with the Mg# of olivine varying from 68 to 95. However, the majority of the fluid released from this reaction was produced within a narrow temperature field of < 30 °C, at higher pressures 2.5 GPa and temperatures 550–600 °C than commonly thought. Fluids derived from the antigorite + brucite reaction might thus trigger eclogite facies equilibration in associated metabasalts, meta-gabbros, meta-rodingites and meta-sediments in the area. This focused fluid release has the potential to trigger intermediate depths earthquakes at 60–80 km in subducted oceanic lithosphere.

**Keywords:** Antigorite + brucite reaction, Olivine, Magnetite, Fluid release, Serpentinites, Eclogite formation, Subduction

## 1 Introduction

Serpentinites are considered as the most important source for water transport in subduction zones (Scambelluri et al. 1995; Ulmer and Trommsdorff 1995). The fluid release upon break down reactions in serpentinites is thought to be responsible for island arc magmatism (Schmidt and Poli 1998), and has the potential to transfer water from hydrous minerals such as brucite

Editorial handling: Paola Manzotti

\*Correspondence: elias.kempf@geo.unibe.ch

<sup>1</sup> Institute of Geological Sciences, University of Bern, Baltzerstrasse 1+3, 3012 Bern, Switzerland

Full list of author information is available at the end of the article



© The Author(s) 2020, corrected publication 2020. This article is licensed under a Creative Commons Attribution 4.0 International License, which permits use, sharing, adaptation, distribution and reproduction in any medium or format, as long as you give appropriate credit to the original author(s) and the source, provide a link to the Creative Commons licence, and indicate if changes were made. The images or other third party material in this article are included in the article's Creative Commons licence, unless indicated otherwise in a credit line to the material. If material is not included in the article's Creative Commons licence and your intended use is not permitted by statutory regulation or exceeds the permitted use, you will need to obtain permission directly from the copyright holder. To view a copy of this licence, visit <http://creativecommons.org/licenses/by/4.0/>.

and antigorite to nominally anhydrous minerals such as metamorphic olivine, likely relevant for the deep water cycle (Kempf and Hermann 2018; Padrón-Navarta and Hermann 2017). The high pressure antigorite breakdown reaction was first suggested at Cima di Gagnone in meta-peridotite lenses by Evans and Trommsdorff (1978). It has been extensively investigated in experimental studies (Bromiley and Pawley 2003; Padrón-Navarta et al. 2010; Ulmer and Trommsdorff 1995; Wunder and Schreyer 1997) but was first described so far in Cerro del Almirez, a unique location in Spain (Padrón-Navarta et al. 2011; Scambelluri et al. 2001; Trommsdorff et al. 1998). Padrón-Navarta et al. (2013) showed that during the antigorite breakdown (antigorite = olivine + enstatite + chlorite + water) 5 wt% of the total rock mass is released as H<sub>2</sub>O. Depending on the bulk rock composition, antigorite + brucite (antigorite + brucite = olivine + chlorite + water) and chlorite-out (chlorite + enstatite = olivine + garnet + water) reactions release between 2 and 3 wt% H<sub>2</sub>O.

While the influence of the terminal breakdown of antigorite on element recycling (Garrido et al. 2005; Harvey et al. 2014; Hermann et al. 2005; Marchesi et al. 2013; Ryan and Chauvel 2014; Savov et al. 2005; Scambelluri et al. 2014, 2019; Spandler and Pirard 2013), subduction zone earthquakes (Dobson et al. 2002; Ferrand et al. 2017; Gasc et al. 2017; Hacker et al. 2003; Jung and Green 2004; Padrón-Navarta et al. 2011; Peacock 2001) and tectonics (Gerya et al. 2002; Guillot et al. 2015) has been widely discussed in the literature, less attention has been paid to the antigorite + brucite reaction (Bloch et al. 2018; Kawahara et al. 2016; Kempf and Hermann 2018; Peretti et al. 1992; Peters et al. 2020; Scambelluri et al. 1991, 1995; Sippl et al. 2019; Spandler et al. 2011), which is frequently exposed in high-pressure ophiolites. Brucite formed during ocean floor serpentinization (Klein et al. 2014) is thought to be produced at low oxygen fugacity conditions (Frost 1985; Peretti et al. 1992). The petrologic importance of brucite in hydrated metaperidotites was first investigated in experimental studies by Bowen and Tuttle (1949). Hostetler et al. (1966) showed its presence in obducted partially serpentinized mantle rocks from circum-Pacific orogenic mountain belts. They pointed out that at first order, the brucite content is controlled by the modal ratio of olivine-orthopyroxene and thus of the Si/Mg ratio of the parent ultramafic rock. Nevertheless, the reaction antigorite + brucite is generally underrepresented in geodynamic models and often ignored (Hacker 2008; Hacker et al. 2003; van Keken et al. 2011). The identification of metamorphic olivine from this reaction is difficult since it often coexists with relic mantle olivine. However, major and minor element signatures were shown to be unique to this type of olivine

(Kunugiza 1982; Nozaka 2003). Moreover, Kempf and Hermann (2018) showed that the presence of brucite enables formation of Si-vacancies in olivine where four hydrogens sit in a tetrahedral site. Therefore, FTIR spectroscopy of metamorphic olivine provides a unique fingerprint to individuate olivine that has formed from the antigorite + brucite reaction.

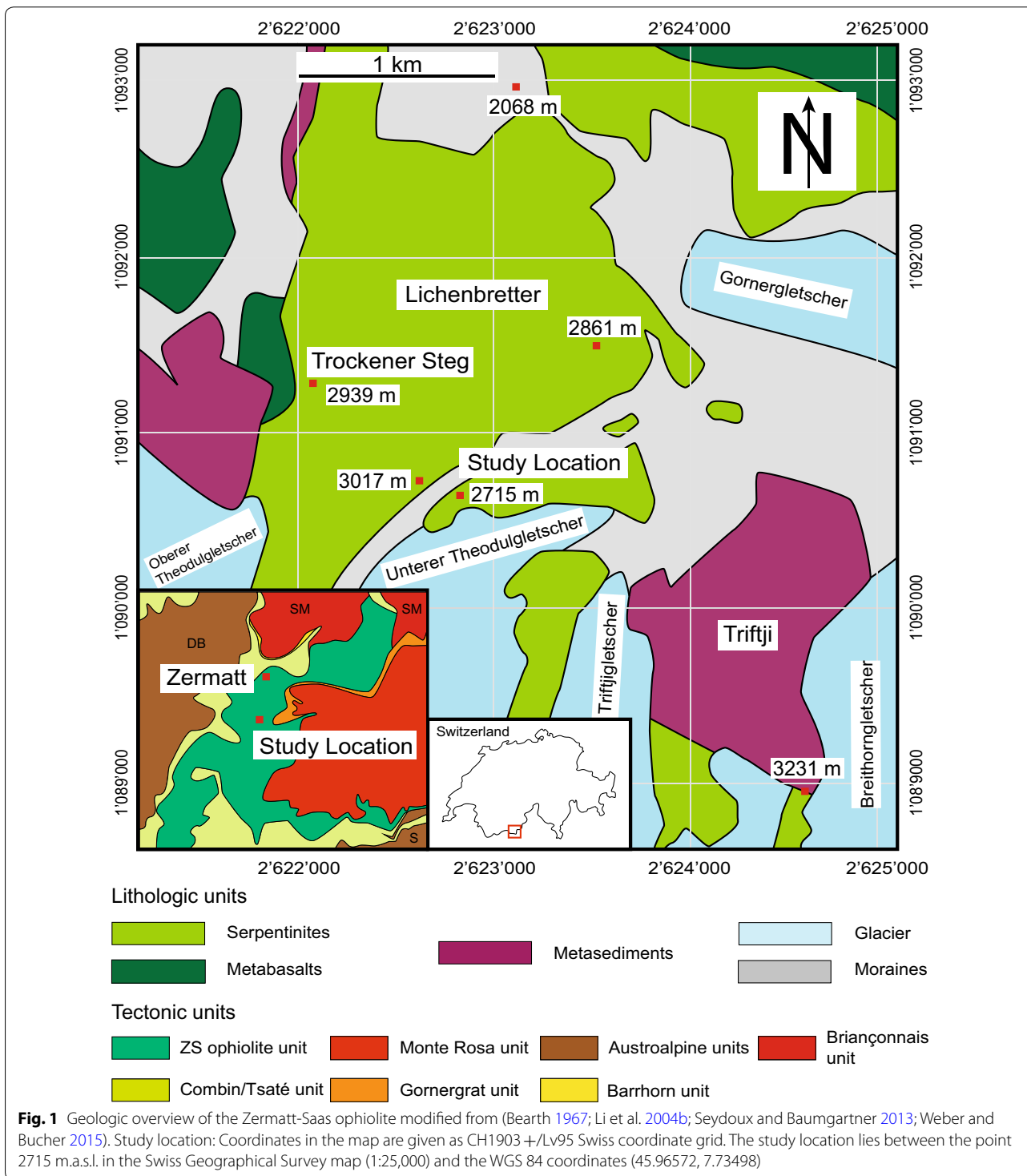
In this study, we investigated in detail an exceptional, glacier-polished outcrop of high-pressure serpentinite in the Zermatt-Saas unit (Switzerland). The outcrop escaped pervasive deformation during the Alpine subduction. We show that a wealth of features related to the hydration of peridotite at the ocean floor as well as the dehydration reaction of antigorite + brucite to olivine during subduction are preserved. This field-based study demonstrates the significance of the olivine-forming reaction for water recycling in subduction zones and its links to subduction related processes.

### 1.1 Geological setting

The Zermatt-Saas high pressure ophiolite belongs to the south Penninic nappe stack system in the western Alps at the border between Switzerland and Italy. It separates the overlying Austroalpine Dent Blanche nappe consisting of continental fragments from the Adriatic crust of the underlying Monte Rosa nappe representing basement fragments derived from the European continental margin (Escher and Beaumont 1997). The ophiolite is a remnant of the middle to late Jurassic (160–120 Ma) Piedmont-Ligurian oceanic lithosphere (Bill et al. 1997; Rubatto et al. 1998) in which the serpentinites represent a hydrated mantle section (Li et al. 2004b). Eclogite facies conditions of 2.2–2.5 GPa and temperatures between 540 and 610 °C are recorded mainly in eclogites associated to the serpentinites (Angiboust et al. 2009; Bearth 1967; Bucher et al. 2005; Bucher and Grapes 2009). The subduction of the oceanic unit occurred 41–49 Ma ago e.g. (de Meyer et al. 2014; Lapen et al. 2003; Rubatto et al. 1998; Skora et al. 2015). The unit was rapidly exhumed within 2–5 My manifested by a greenschist facies overprint at 400–500 °C and 0.4–0.6 GPa (Agard et al. 2009; Cartwright and Barnicoat 2002; de Meyer et al. 2014; Reinecke 1991; Rubatto et al. 1998; Skora et al. 2015). The serpentinite covers 30 km<sup>2</sup> in the Zermatt area and shows massive and mylonite structures (Li et al. 2004b). Meta-mafic dykes within the serpentinites are abundant and most prominently represented by metarodingites (Li et al. 2004a; Li et al. 2008). Since the southern portion of the serpentinites in the Zermatt area are located at high altitudes (2300–4100 m.a.s.l.) large parts were covered by glaciers. During the past decades glacial retreat has uncovered

new outcrops at higher altitudes. Their investigation is particularly instructive since the wall rock is smoothly abraded and, unlike most serpentinites in the area, shows hardly any surface weathering. This study focuses on an exceptional, ~100 × 100 m outcrop,

close to the Unterer Theodulglacier that escaped mylonitic deformation (Fig. 1) and preserves a full orogenic cycle from mantle exhumation to seafloor hydration, subduction and exhumation.



## 2 Analytical methods

Polished thin sections (approximately 30  $\mu\text{m}$  thickness for FA, MF, AF2, ME, O11, O12, O126, O146) were produced from representative samples and textures were investigated by optical microscopy, BSE imaging and quantitative WDS mapping. A subset of these samples were analysed also with LA-ICP-MS for trace elements. Fourier transform infrared (FTIR) spectroscopy measurements on olivine were obtained in 100–200  $\mu\text{m}$  thick sections for H<sub>2</sub>O analyses. The locations of all samples are shown in Fig. 2 and the full sample list is presented in Additional file 1: Table S1.

### 2.1 Electron probe micro analyser (EPMA)

A JEOL JXA-8200 Superprobe equipped with five wavelength dispersive crystal spectrometers (WDS) and one energy dispersive spectrometer (EDS) housed at the Institute of Geological Sciences, University of Bern was used for quantitative spot analyses and X-ray mapping. A backscatter detector (BSE) was used for imaging and micro-textural analyses. Samples were measured with 15 kV acceleration voltage and 20 nA probe current. Measurement time included 20 s on the peak and 10 s on background positions on either side of the peak. Natural and synthetic oxide and silicate minerals were used as standards. X-ray maps were acquired using a pixel size of 2  $\mu\text{m}$ , a dwell time of 200 ms and a probe current of 100 nA. Spot analyses used as standards for the map quantification were acquired prior to mapping with the WDS spectrometers. Maps were processed, calibrated and analysed using the software XMAP-TOOLS (Lanari et al. 2014, 2019).

### 2.2 Laser ablation inductively coupled mass spectrometry (LA-ICP-MS)

Trace element analyses were measured by LA-ICP-MS using a Geolas Pro 193 nm ArF excimer laser with an ELAN DRC-e quadrupole ICP-MS. Optimization of the instrument followed the strategy protocol of Pettke et al. (2012). The mass spectrometer was optimised on NIST 610 and 612 glasses and the GSD-1G glass was used as an external standard. The laser fluence was set to 6 J·cm<sup>-2</sup> with a repetition of 10 Hz. Spot diameters were chosen as large as possible between 60 and 120  $\mu\text{m}$ . Background measurements lasted 50 s before each set whereas >30 s measurement intervals were integrated and recalculated to element mass. MgO was used as an internal standard from quantitative EPMA analyses and the MATLAB®-based programme SILLS was used for data reduction (Guillong et al. 2008).

### 2.3 Fourier transform infrared spectroscopy (FTIR)

For FTIR measurements, 200/100  $\mu\text{m}$  thick sections were analysed. Only inclusion free olivine grains were measured with a MCT (Mercury-Cadmium-Telluride) detector. The water maps were measured using a FPA (Focal Plane Array) detector. A total of 4096 acquired spectra (for a detailed description see Data Directory of Kempf and Hermann (2018)) were corrected for base-line and atmospheric water compensation using the Opus<sup>®</sup> software. Spectra obtained by MCT and FPA were renormalized to 1 cm thickness. For single-spot measurements (MCT) thicknesses of the samples were determined with a probe (dial) indicator having an accuracy of 1  $\mu\text{m}$ . FPA maps were thickness corrected with the integrated overtones (Shen et al. 2014) and the water contents were recalculated with the Bell et al. (2003) absorption coefficient. For a more detailed description see Kempf and Hermann (2018).

## 3 Results

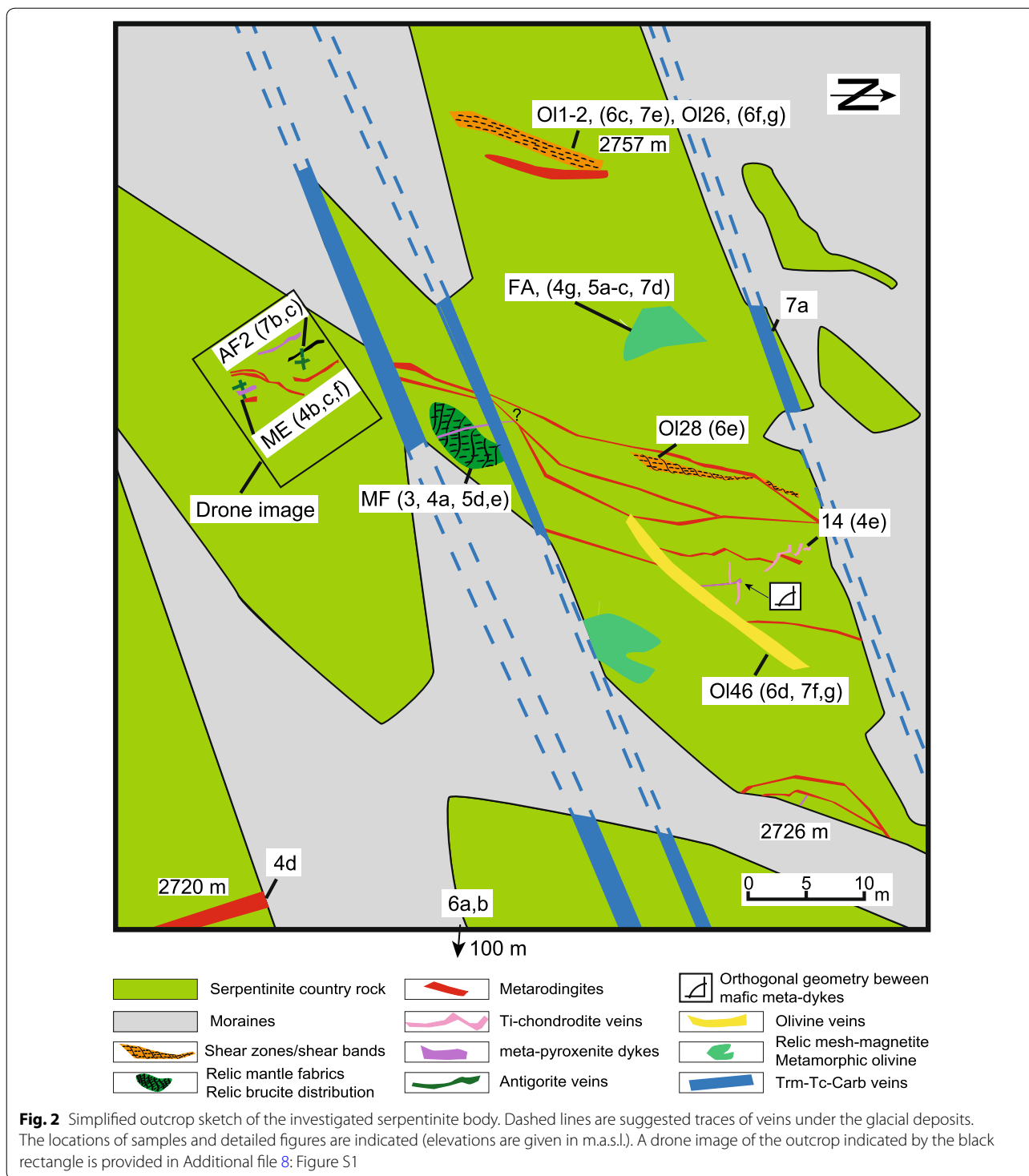
### 3.1 Field relations and sample descriptions

All the samples were collected from a continuous outcrop within an area of 100 × 100 m on glacially polished serpentinites partially covered by glacial debris (moraine). The outcropping rocks were only weakly affected by Alpine deformation. In Fig. 2, the main lithological and structural elements are presented schematically. Various meta-dykes and vein sets show cross-cutting relationships that are visible at the map scale (Fig. 2). The location of the important samples and references to outcrop photos are also shown on the map. In the following, the main features are described chronologically based on mineralogy, cross-cutting and overprinting relationships.

Mineral abbreviations are only used in Figures: Brucite (Bc), Ti-clinohumite (Ti-cl), Ti-chondrodite (Ti-ch), Magnetite (Mt), Calcite (Cc), Andradite (Andr), Uvarovite (Uvar), Cr-magnetite (Cr-Mt), Tremolite (Trm), Talc (Tc), Chrysotile (Chr), Cr-spinel (Cr-spin), Perovskite (Prv), Sulphide (Sulph). All other mineral abbreviations follow Whitney and Evans (2010).

#### 3.1.1 Evidence for relic mantle fabrics

In the serpentinite least affected by Alpine deformation (Fig. 3) several centimetre large and parallel oriented, stretched chromites are embedded in a statically grown antigorite-olivine matrix and are aligned along a preferred orientation constituting the pre-Alpine tectonite foliation (Fig. 3a). Occasionally, chromite contains three compositionally distinct zones consisting of brown Cr-spinel under polarised light, enclosed by Cr-magnetite rich in chlorite inclusion, and a magnetite-rich rim (Fig. 3b, c Table 1). The brown Cr-spinel is the



only pre-oceanic relic phase observed in these rocks. No relic of mantle olivine was found. All olivines in these rocks are related to Alpine metamorphism, based on textures and composition (see below).

### 3.1.2 Intrusion of mafic dykes

The tectonite foliation (Fig. 4a) is crosscut by meta-pyroxenite dykes of several centimetre thickness and several meters up to tens of meters length (Fig. 4a, b),

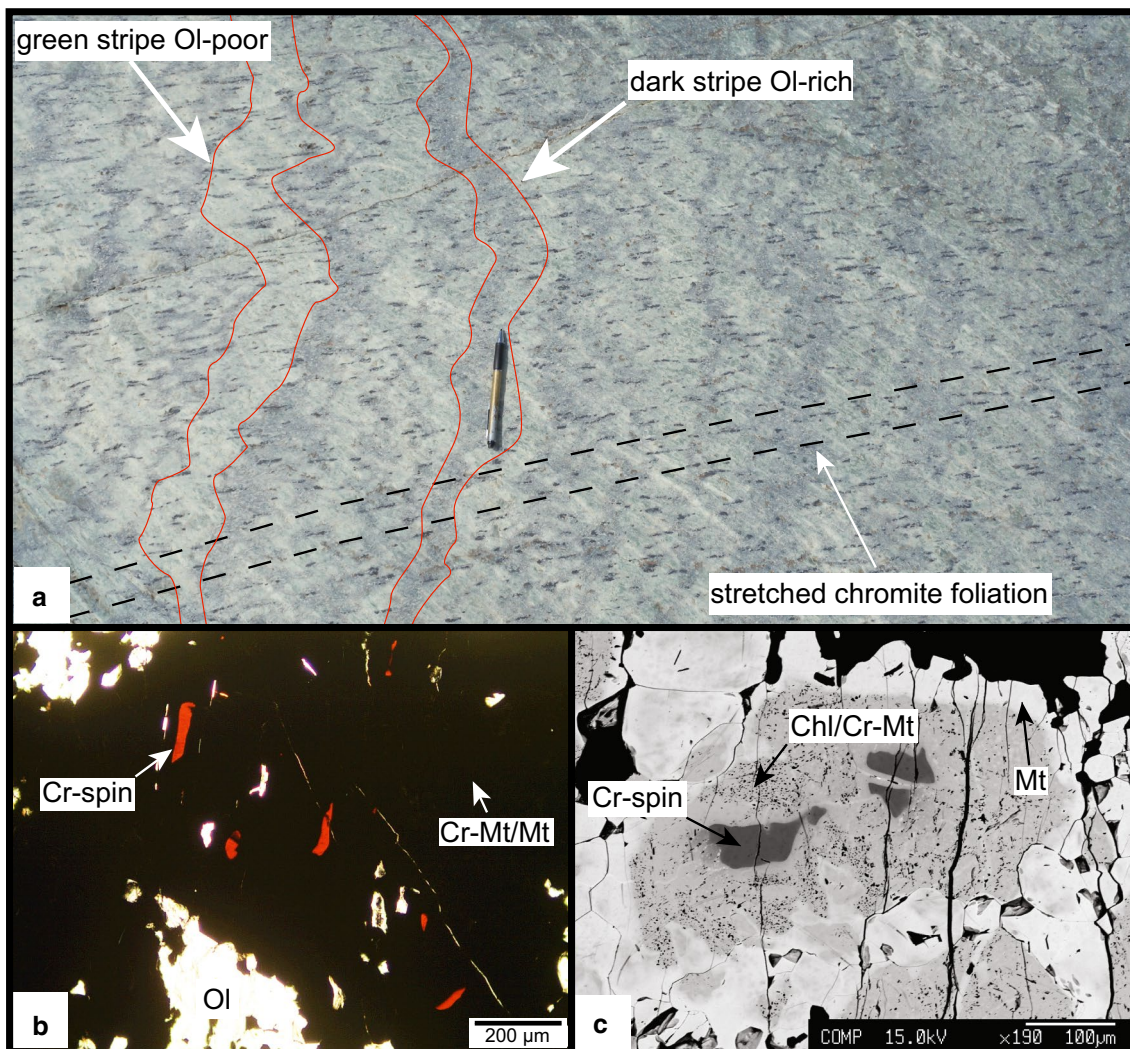


**Fig. 3** **a** Antigorite-olivine-chlorite serpentinite with large stretched chromites defining the pre-alpine foliation (samples MF and OI28, see Fig. 2 for position, scale ~15 cm). **b** Polarised light image, with brown Cr-spinel relics in chromites (sample OI28). **c** BSE image showing Cr-spinel core, Cr-magnetite and magnetite rims (sample OI28)

surrounded by an olivine and magnetite-rich but chromite poor halo. Occasionally, in the meta-dyke interiors relic pyroxenes are preserved (Fig. 4c). Most prominent are metarodingites consisting of epidote, grossular-rich garnet, diopside and titanite (Fig. 4d) that are tens of metres long and occasionally over one metre thick. The rodingites are enclosed by chlorite blackwalls with minor magnetite and rare perovskite. Less abundant red-brown veins consisting of Ti-chondrodite are nearly perpendicular to the metarodingites and meta-pyroxenites (Figs. 2, 4e). These veins and the rodingites are mutually crosscutting, i.e. in places the rodingite cross-cuts the Ti-rich veins and in other places the Ti-rich veins cross-cut the rodingite. Both cut the tectonite foliation and are

boudinaged in areas with strong Alpine serpentine mylonitization. From this observation we conclude that the rodingite represents primitive mafic dykes whereas the Ti-chondrodite veins originate from more evolved Fe-Ti gabbroic or basaltic dykes (Gilio et al. 2019). The pervasive rodingitisation provides evidence for extensive fluid-rock interaction between the exhumed peridotites, mafic dykes and a seawater-derived fluid (Li et al. 2004a, b).

### 3.1.3 Oceanic serpentinization

The tectonite foliation and undeformed serpentinites are also crosscut by veinlets consisting of light to dark green serpentine associated with carbonates (Fig. 5a). Serpentinization of mantle olivine involves the formation of the

**Table 1 Major and minor element composition of magnetite, Cr-magnetite, Cr-spinel**

Sample	FA					OI28				MF	OI26
	Polygon	Vein	Core	Core	Rim	Core	Core	Rim	Core	Polygon	Vein
TiO <sub>2</sub>	0.05	0.06	0.14	0.12	0.06	0.14	0.15	0.04	0.20	0.06	0.12
Al <sub>2</sub> O <sub>3</sub>	b.d.	0.15	0.27	0.03	0.03	4.38	0.23	0.01	26.82	0.09	0.02
Cr <sub>2</sub> O <sub>3</sub>	1.55	3.94	24.53	8.11	4.06	35.95	45.78	3.15	40.34	3.08	1.03
Fe <sub>2</sub> O <sub>3</sub>	68.81	67.14	46.33	63.07	66.40	31.90	27.39	67.10	4.50	67.80	69.10
FeO	24.60	23.49	15.62	21.62	24.04	15.93	15.87	25.61	10.51	23.07	24.07
MnO	0.31	0.58	2.77	0.82	0.45	2.16	2.86	0.23	1.45	0.44	0.46
NiO	0.32	0.29	0.24	0.37	0.23	0.19	0.06	0.33	0.06	0.64	0.43
MgO	3.70	4.47	7.92	5.50	4.07	9.24	8.64	3.16	15.89	4.06	3.96
CaO	b.d.	0.01	0.59	b.d.	0.01	b.d.	0.01	0.02	0.01	b.d.	b.d.
Total	99.35	100.15	99.01	99.71	99.36	99.93	101.05	99.68	99.79	99.45	99.28
Ti	0.002	0.002	0.004	0.003	0.002	<0.001	0.040	<0.001	<0.001	0.002	0.003
Al	–	0.007	0.011	0.001	0.001	0.180	0.001	<0.001	0.940	0.004	0.001
Cr	0.046	0.116	0.698	0.237	0.120	0.980	1.263	0.090	0.950	0.091	0.031
Fe <sup>3</sup>	1.950	1.873	1.254	1.751	1.873	0.830	0.719	1.900	0.100	1.909	1.955
Fe <sup>2</sup>	0.775	0.728	0.470	0.667	0.754	0.460	0.463	0.810	0.260	0.722	0.757
Mn	0.010	0.018	0.084	0.026	0.014	0.060	0.085	0.010	0.040	0.014	0.015
Ni	0.010	0.009	0.007	0.011	0.007	0.010	0.002	0.010	<0.001	0.019	0.013
Mg	0.208	0.247	0.425	0.302	0.227	0.480	0.449	0.180	0.700	0.226	0.222
Ca	–	<0.001	0.023	–	<0.001	–	<0.001	<0.001	<0.001	–	–
Mg#	20.7	24.7	43.1	30.1	22.7	47.5	42.2	17.8	70.0	23.1	22.0
Cr#	1.000	0.946	0.984	0.994	0.989	0.845	0.961	1.000	0.503	0.957	0.965

CaO and SiO<sub>2</sub> mass fractions derive from secondary fluorescence and or beam deflection

Normalized to 3 cations and 4 oxygens Mg# = (Mg/(Mg + Fe + Ni + Mn))\*100

Cr# = Cr/(Cr + Al)

b.d. below detection limit

characteristic mesh textures consisting of magnetite polygons filled with serpentine minerals and brucite (Evans 2004; O'Hanley 1996; Wicks and Whittaker 1977). In the least deformed rocks magnetite polygons are well preserved in both olivine-free and olivine-bearing serpentinites (Figs. 4f, 5b, c, d). The mesh texture is frequently accompanied with up to millimetre wide magnetite veins (Fig. 5c), commonly interpreted as conduits of aqueous fluid (Frost and Beard 2007). Antigorite domains with no magnetite mesh textures are interpreted to derive from former orthopyroxene (Fig. 4f). Hydration of mantle Cr-spinel (Fig. 3b, c) involves the formation of two distinct rims. The first consists of Cr-magnetite containing

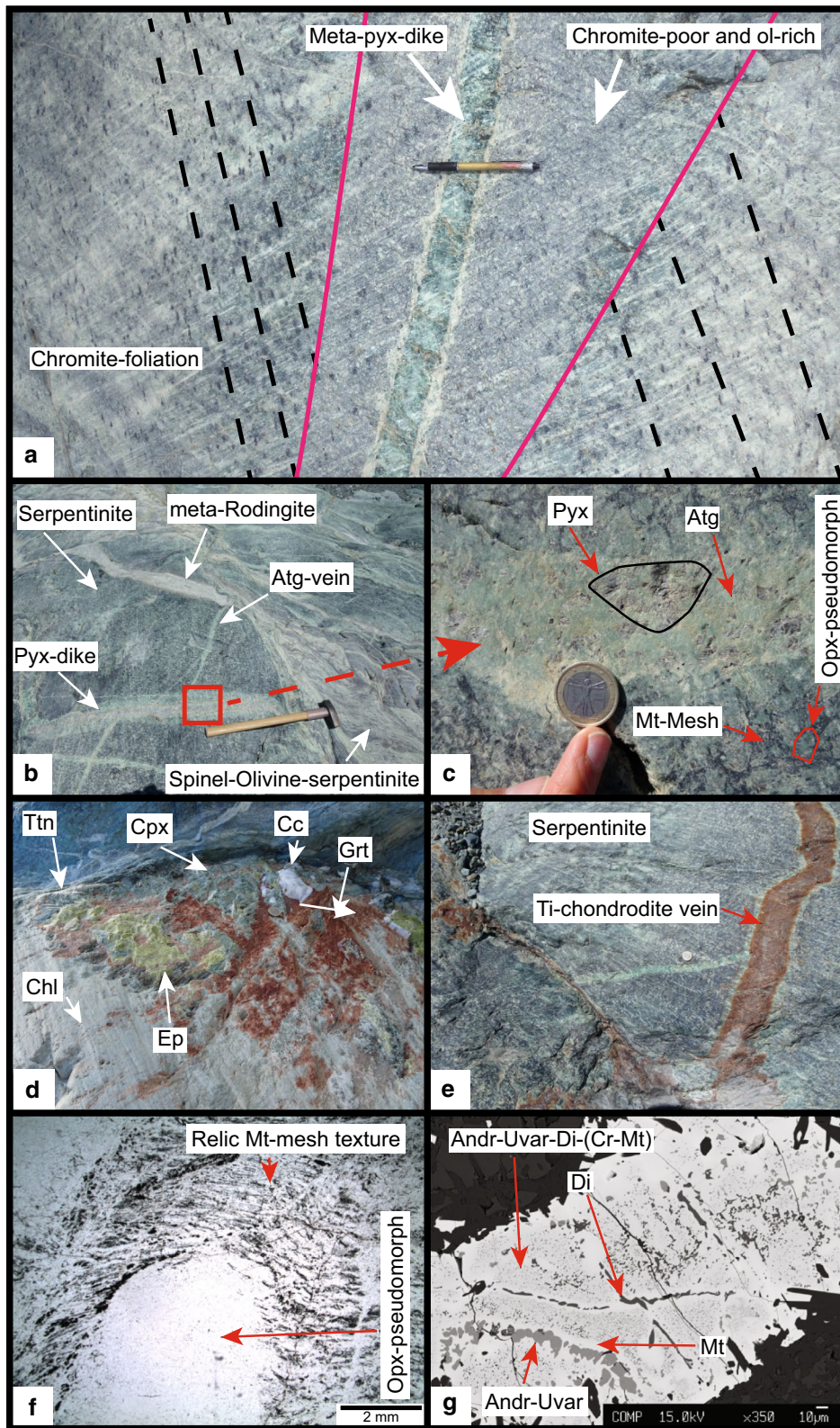
chlorite inclusions that are surrounded by later magnetite. During serpentinization, Ca metasomatism transformed the basaltic dykes into rodingites (Li et al. 2004a). In the serpentinites, Ca-mobility is manifested by the intergrowth of andradite and diopside with Cr-magnetite and magnetite (Fig. 4g). This association is well known in serpentinites and develops at very low oxygen fugacity together with FeNi-alloys (Frost 1985; Frost and Beard 2007).

### 3.1.4 Metamorphic olivine formation

Olivine is widespread in the serpentinites and appears either as darker shadings in very fresh outcrops where

(See figure on next page.)

**Fig. 4** **a** Meta-mafic dyke generation<sub>1</sub> crosscutting the chromite foliation with an olivine-rich and spinel-poor halo. **b** Serpentinite containing several meta-dyke (vein) generations (sample ME, see Fig. 2 for position) (Hammer scale length, ~60 cm). **c** Meta-pyroxenite dyke (vein) mostly serpentinized containing relic pyroxene (Euro coin 2.3 cm diameter). **d** Metarodingites showing the typical assemblage diopside, grossular and epidote in the core and chlorite at the rim together with titanite and calcite (Fig. 2). **e** Ti-chondrodite vein (meta-Ti-gabbro/basalt dyke) in serpentinite (sample 14). **f** Mt-mesh from serpentinized mantle olivine and antigorite pseudomorph after orthopyroxene (sample ME). **g** Andradite-uvarovite and diopside finely disseminated in partially replaced Cr-magnetite (sample FA)



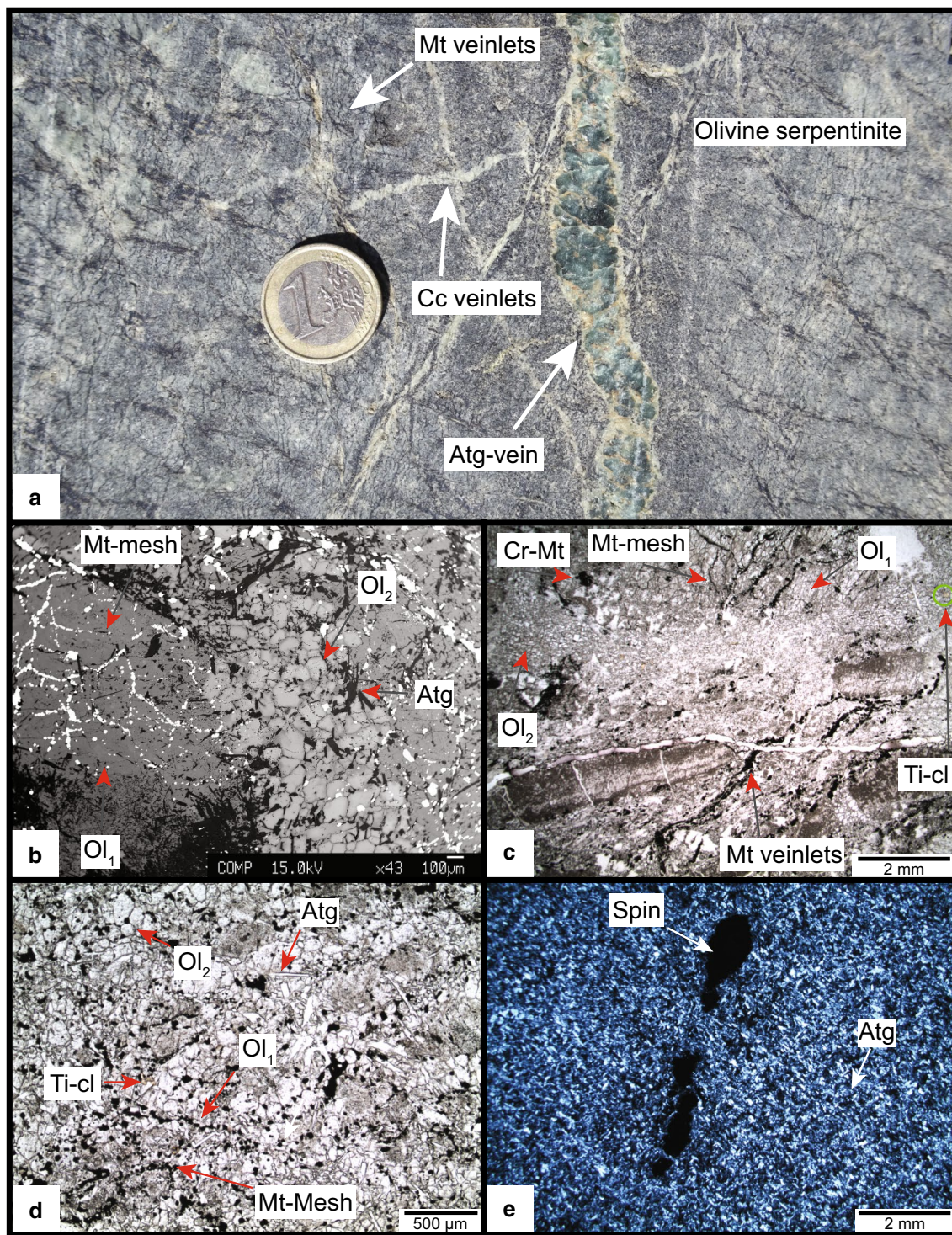


**Fig. 5** **a** Country rock sample FA (Fig. 2 for position) with grey-white olivine, black magnetite veinlets and cross-cutting antigorite and calcite veins (Euro coin 2.3 cm diameter). **b** Backscatter image of a large olivine<sub>1</sub> enclosing the magnetite mesh texture. Small idioblastic olivines form the mosaic texture with antigorite. Note the partial or full disappearance of magnetite veins and mesh polygons in this domain (sample MF). **c** Thin section image (plain polarized light) of olivine<sub>1</sub>- and recrystallized olivine<sub>2</sub> domains, note the absence of magnetite veins and mesh textures in domain<sub>2</sub> (sample FA). **d** Plain polarised light image from a dark stripe consisting of large inclusion-rich olivine<sub>1</sub> with magnetite polygons and idioblastic olivine<sub>2</sub> forming a mosaic texture with antigorite (sample MF). **e** Crossed polarised light image of a green stripe (**a**) consisting of interlocked antigorite and relic chromites (sample MF)

the glacier retreat was recent (Figs. 3a, 5a) or with an orange weathering colour in outcrops that have been exposed for a longer time. Olivine formation is best studied in sample FA (Fig. 5). Macroscopically, the FA rock is massive dark grey with sub-millimeter wide and several tens of centimetre long magnetite veins. The magnetite mesh texture and magnetite veins are overgrown by 0.5–2 cm large olivine<sub>1</sub> (Fig. 5b, c, d) providing textural evidence for a metamorphic origin of the olivine post-dating oceanic magnetite formation. This large olivine<sub>1</sub> is partially recrystallized in sub-parallel bands (Fig. 5b, c) consisting of 50–200 micron sized polygonal olivine<sub>2</sub> associated to Ti-clinohumite grains, forming a mosaic texture with antigorite and occasionally chlorite (Fig. 5b, c, d). In these mosaic domains, magnetite veins as well as the mesh texture are marginally offset and disappear (Fig. 5c). Opaque phases such as sulphides occur as inclusions in olivine<sub>1</sub> and are absent in the mosaic domain (Fig. 5c, for sulphides see Additional file 2: Figure S2, see Piccoli et al. (2019)).

### 3.1.5 Shear zones and olivine veins

Occasionally, sub-centimetre to several centimetre wide, olivine-rich veinlets of the olivine<sub>2</sub>-domain merge to form olivine-rich shear zones, which range from a few tens of centimetres to over 1 m thickness and are up to several tens of metres long (Fig. 6a). Idioblastic olivine grains show diameters of 100–500 microns and form a mosaic texture with variable amounts of chlorite, antigorite and Ti-clinohumite/Ti-chondrodite (Fig. 6b, c). Olivine veins are several centimetres wide and up to 1 m long. They often occur en-echelon in sheared domains (Figs. 2 and 6d, e) and contain up to several centimetre large single crystal olivines (Fig. 6d), few Ti-clinohumite grains and variable amounts of white diopside. Moreover, in an olivine vein juxtaposed to a metarodingite accessory andradite and perovskite (Fig. 6f, g) are present.

### 3.1.6 Retrograde features

Late tremolite-actinolite-talc-carbonate veins crosscut the prograde olivine-bearing serpentinite. The veins are several tens to hundreds of meters long and up to 2 m wide. Three large talc-magnesite veins are present in the centre of the outcrop (Fig. 2). The veins show a serpentinized (antigorite) halo at the contact to the olivine-rich-serpentinites (Fig. 7a). Also, 1–3 cm wide and up to

several metres long antigorite veins crosscut the olivine-serpentinites and olivine-magnetite veins (Fig. 7b) pseudomorphically replacing olivine grains (Fig. 7c, sample AF2). Late brucite, lizardite/chrysotile (Chr/Lz), magnetite and sulphide minerals occasionally co-precipitated with calcite veins crosscut and replace prograde olivine (Fig. 7d (FA), e (OI1-2), f, g (OI46)). Additionally, olivines recrystallize to higher Mg# while magnetite co-precipitates (Fig. 7g and Table 2).

### 3.1.7 Summary of the main stages derived from field observations

The single outcrop preserves a complete history of extension and convergence related to the formation, subduction and exhumation of oceanic lithosphere during the Alpine orogeny. Mantle exhumation is documented by chromite in a tectonite foliation followed by intrusions of mafic dykes close to the ocean floor. Oceanic hydrothermal alteration produced a pervasive serpentinization coupled with magnetite formation and rodingitisation of mafic dykes. Alpine subduction, prograde metamorphism, and limited deformation is best documented in metamorphic olivine that occurs either statically in undeformed parts or dynamically in shear zones and en-echelon veins. Late, crosscutting veins are related to the exhumation of the rocks.

### 3.2 Mineral compositions

Major and minor element compositions from the three most important localities of the olivine forming reactions i.e., the country rock (MF, OI28, FA, AF2), a shear zone (OI1-2) and olivine veins (OI26, OI46) are reported in Table 2 and Fig. 8a. Trace elements in olivine are documented in Table 3 and Fig. 8b. Major and minor element compositions of antigorite and chlorite are given in Table 4 and of Ti-chondrodite and Ti-clinohumite in Table 5. Data from minor and accessory phases such as, andradite-uvarovite garnet, ilmenite, perovskite, brucite, lizardite/chrysotile and clinopyroxene are presented in Table 6. The full data set for all phase compositions used in this paragraph is given in Additional file 3: Table S2.

#### 3.2.1 Spinel

The brown Cr-spinel cores in sample OI28 (Table 1) lie on the compositional line between Cr and Al endmember at Cr# 0.5 typical for upper mantle compositions

(See figure on next page.)

**Fig. 6** **a** Olivine-rich shear zone (Fig. 2 for position) with indicated sense of shear (hammer scale length: 60 cm). **b** Zoom-in of **a**, showing the presence of Ti-clinohumite in addition to olivine. **c** Ti-chondrodite grain replaced by Ti-clinohumite in an olivine-rich matrix (sample OI1) (Euro coin 2.3 cm diameter). **d** Olivine vein consisting of centimetre sized single crystal olivines, interstitial diopside and red-brown Ti-clinohumite (Finger scale 8 cm). **e** Olivine shear bands, with indicated sense of shear. **f** Backscatter image of a large olivine showing the presence of andradite, diopside, magnetite and perovskite (**g**) (both sample OI26)

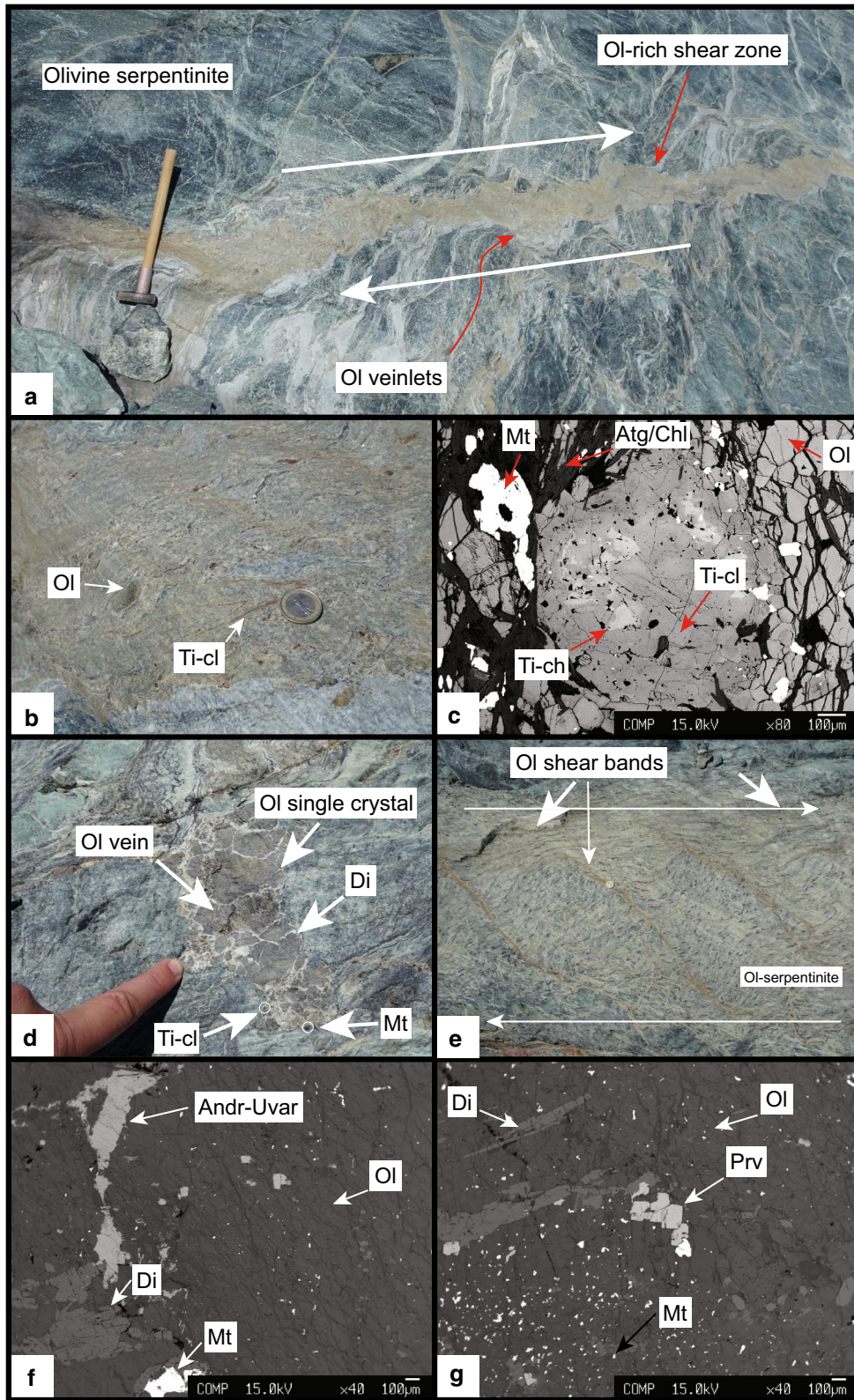


(Fig. 9). Cr-magnetite surrounding or replacing Cr-spinel (Fig. 3b, c) in FA and Ol28 shows elevated  $\text{Cr}_2\text{O}_3$  contents of 25–46 wt% (Table 1). The recrystallized chromite rims magnetite veins and polygons contain only 1–4 wt%  $\text{Cr}_2\text{O}_3$  (Table 1).

### 3.2.2 Olivine

Olivines from all studied samples including country rocks (AF2, MF, Ol28, FA), shear zone Ol1–Ol2 and olivine veins (Ol26, Ol46) show high Mg# 94–95 in the cores (Table 2, Figs. 8a, 10). The first generation olivine<sub>1</sub> consisting of large olivine grains shows erratic patches of concentrically zoned Mg# 95–97 from core to rim and decreasing Ni with increasing Mg# (Figs. 8a, 10b). The second generation, olivine<sub>2</sub>, shows different populations among different samples with on average lower Mg# 94–95, but similar Ni contents compared with olivine<sub>1</sub> (Fig. 8a). Trace element measurements of olivine<sub>1</sub> returned mixed analyses due to the presence of numerous mineral inclusions. Successful analyses were only possible in clear, recrystallized olivine<sub>2</sub> in samples FA, Ol1, Ol2 and Ol26. The trace element content relative to primitive mantle is very low in olivine<sub>2</sub> (Fig. 8b), only B shows >10 fold enrichment. Values for Li, Sc, Co, Ni and Zn are close to primitive mantle compositions, Mn is roughly two fold increased, whereas the remaining elements including the HREE are depleted (Fig. 8b). Al-contents range from 0.3 to 0.41  $\mu\text{g/g}$ , whereas Cr-contents vary between 3.3 and 9.25  $\mu\text{g/g}$  (Table 3).

### 3.2.3 Antigorite and chlorite

Our analyses were focussed on antigorite in textural equilibrium with olivine that formed close to peak metamorphic conditions or during early stages of retrogression. The serpentine generation occurring locally as late replacement veins (Fig. 7b, c) or halos (Fig. 7a) are volumetrically not important and not further considered here. Antigorite was recalculated to the polymorph  $m=17$  (Mellini et al. 1987). It shows core-to-rim zoning with elevated mass fractions of 2.2–2.8 wt%  $\text{Al}_2\text{O}_3$  and 0.5–1.7 wt%  $\text{Cr}_2\text{O}_3$  in the prograde cores and lower values at rims with little variation of Mg# 97–98 (Table 4). The rims developed coevally with late stage retrograde serpentine formation (Table 4). Decreasing Al-contents from core

to rim are visible in the compositional map (Fig. 10f). Moreover, chlorite-bearing samples such as FA, Ol1-2, and Ol46 show generally higher  $\text{Al}_2\text{O}_3$  mass fractions in antigorite than in chlorite-absent samples such as MF (Table 4). Chlorite contains 11–13 wt%  $\text{Al}_2\text{O}_3$ , between 0.7 and 2.6 wt%  $\text{Cr}_2\text{O}_3$  and Mg# 95–96 in FA, Ol1-2, and Ol46 samples (Table 4, Fig. 10a, e).

### 3.2.4 Other minerals

A single Ti-chondrodite grain from the shear zone (Ol1) shows Mg# 96 and contains 8.7 wt%  $\text{TiO}_2$  (Table 5, Fig. 6c). Large grains from a Ti-chondrodite vein (sample 14) show Mg# 92–93 and  $\text{TiO}_2$  contents between 8.35 and 9.14 wt%. Small idioblastic grains in the Ti-chondrodite vein have Mg# 94 and  $\text{TiO}_2$  contents of 8 wt% (Table 5). Ti-clinohumites have Mg# 94–97 in Ol26, FA, AF2, Ol46 and MF and retrograde rims replacing Ti-chondrodites in the vein Mg# 95–96.  $\text{TiO}_2$  values vary between 2.1 and 4.9 wt% (Table 5). Both clinopyroxene (diopside) inclusions in olivine (sample FA) and the large grains in olivine veins (Ol26) show near endmember compositions with Mg# 98–99. Garnet in the country rock sample associated with Cr-magnetite and magnetite (FA) is characterised by a 60 mol% component of andradite and a 40 mol% component of uvarovite (Table 6). The garnet present in the olivine vein Ol26 consists of 91 mol% andradite and contains a small grossular component of 8 mol%. Ilmenite in sample 14 (Additional file 4: Figure S3) consists of 54–69 mol% geikilite and 16–35 mol% ilmenite endmembers and contain 4–6 mol% hematite and a 6–9 mol% Mn-ilmenite component. Perovskite grains in the olivine vein Ol26 show close to endmember compositions (Table 6). Retrograde brucite has Mg# 94–96 and is associated with lizardite/chrysotile of Mg# 97 and occasionally magnetite and calcite veins.

### 3.3 Quantitative compositional mapping

An element distribution map was obtained from sample FA (Fig. 10a–d; see Additional file 5: Figure S4 for thin section image) that documents best the different olivine generations. The map is divided into two domains. In the right domain a large olivine<sub>1</sub> grain contains inclusions of antigorite and chlorite and overgrows relic magnetite mesh textures (Fig. 10a, b). In the left domain, chlorite

(See figure on next page.)

**Fig. 7** **a** Tremolite-talc-carbonate vein crosscutting olivine-rich country rock, note the serpentinization front (Fig. 2 for position). **b** Antigorite vein crosscutting an olivine-magnetite vein and the olivine-rich country rock (sample AF2). **c** Thin section image of **b** showing the pseudomorphic replacement of antigorite after olivine (sample AF2). **d** Late carbonate vein formation together with brucite, lizardite/chrysotile and magnetite (sample FA). **e** Brucite and lizardite/chrysotile veins crosscutting olivine in a shear zone (sample Ol1-2). **f** Calcite vein crosscutting a large olivine single crystal, note the coincidence of brucite and lizardite/chrysotile, magnetite-rich rims and low Mg# in the olivine in contact (sample Ol46). **g** Large blades of antigorite included by large olivine<sub>2</sub> crystal which is partially replaced with higher Mg# olivine veinlets extending from veins with brucite and lizardite/chrysotile (sample Ol46)

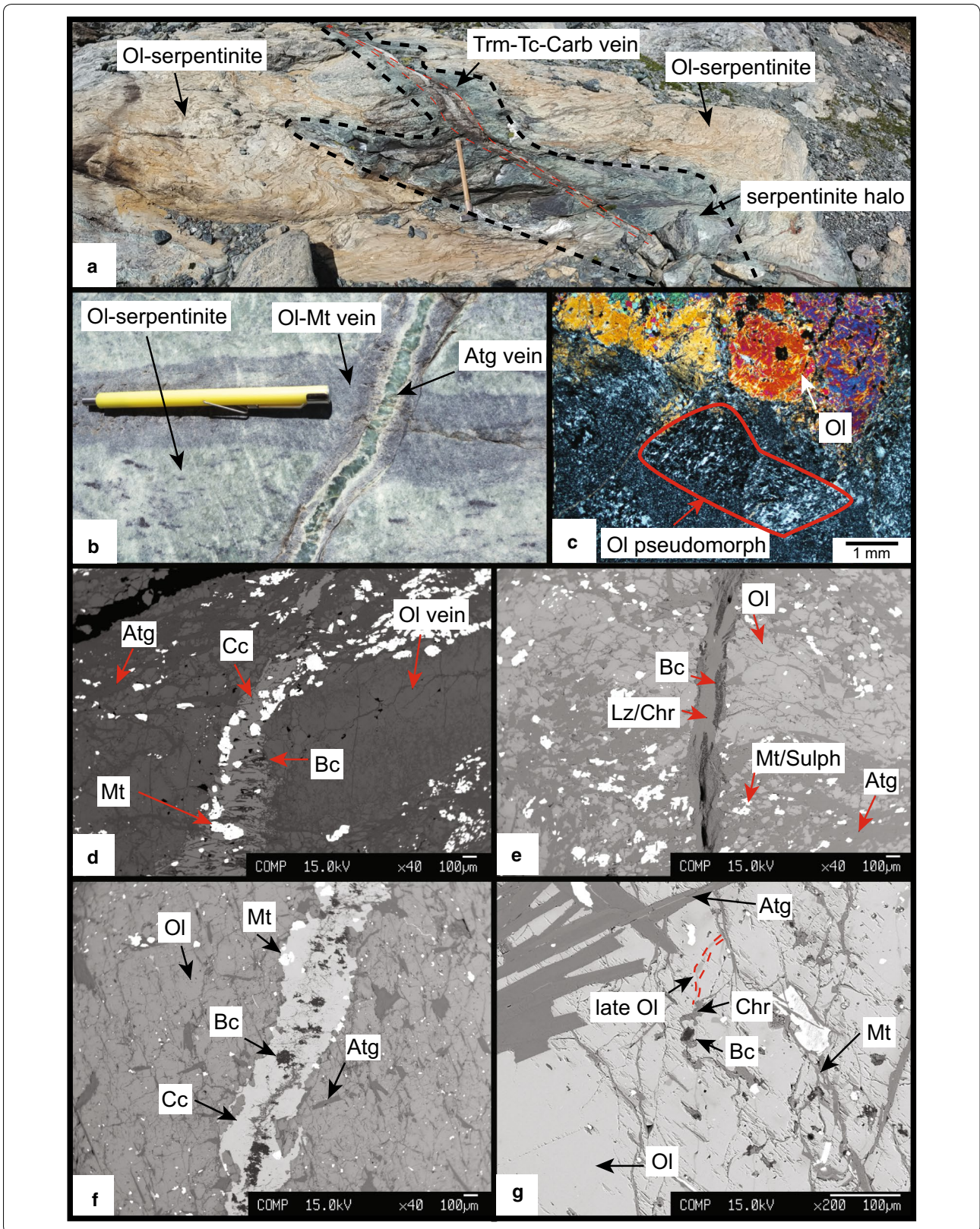


**Table 2 Major and minor element composition of olivine**

Sample	O11		O12		FA		MF		O128		O126		O146		AF2		
	2	Core	2	Core	2	Core	1	2	1	2	1	2	1	2	1	2	
wt%																	
SiO <sub>2</sub>	41.59	41.43	42.05	42.31	42.61	41.50	41.17	42.14	41.90	41.49	41.62	41.79	41.69	41.95	42.21	42.59	
TiO <sub>2</sub>	b.d.	b.d.	0.02	0.07	0.01	b.d.	b.d.	b.d.	0.02	b.d.	0.05	b.d.	0.02	0.01	0.01	0.04	
Al <sub>2</sub> O <sub>3</sub>	b.d.	0.03	0.08	0.01	0.02	0.01	0.04	0.07	b.d.	b.d.	0.02	b.d.	0.01	0.01	0.02	b.d.	
Cr <sub>2</sub> O <sub>3</sub>	0.01	b.d.	0.01	0.02	0.03	0.01	b.d.	0.01	0.01	b.d.	b.d.	b.d.	0.01	b.d.	0.01	0.01	
FeO	4.66	4.60	4.58	4.21	2.40	5.34	5.23	2.15	4.58	4.63	4.72	5.40	3.93	5.25	4.64	2.25	
MnO	0.29	0.24	0.20	0.20	0.22	0.21	0.21	0.23	0.16	0.27	0.31	0.36	0.18	0.23	0.23	0.28	
NiO	0.16	0.15	0.18	0.22	0.13	0.23	0.17	0.15	0.17	0.15	0.16	0.22	0.17	0.27	0.21	0.19	
MgO	53.30	53.64	53.68	53.99	54.90	52.97	53.06	54.85	53.48	53.07	52.84	52.95	54.04	53.19	53.10	55.53	
CaO	b.d.	b.d.	0.02	0.01	b.d.	b.d.	0.01	b.d.	0.03	0.01	0.01	b.d.	0.01	0.01	0.01	b.d.	
Total	100.01	100.10	100.82	101.04	100.32	100.28	99.90	99.60	100.34	99.63	99.73	100.72	100.07	100.92	100.45	100.88	
Si	0.997	0.992	0.999	1.001	1.006	0.995	0.991	1.002	1.000	0.998	1.000	0.998	0.995	0.999	1.006	1.000	
Ti	-	-	<0.001	0.001	<0.001	-	-	-	<0.001	-	<0.001	-	<0.001	<0.001	<0.001	0.001	
Al	-	0.001	0.002	<0.001	0.001	<0.001	0.001	0.002	-	-	<0.001	-	<0.001	<0.001	0.001	-	
Cr	<0.001	-	<0.001	<0.001	0.001	<0.001	-	<0.001	<0.001	-	-	-	<0.001	-	<0.001	<0.001	
Fe <sup>+2</sup>	0.093	0.092	0.091	0.083	0.047	0.107	0.105	0.043	0.091	0.093	0.095	0.108	0.079	0.105	0.093	0.044	
Mn	0.006	0.005	0.004	0.004	0.004	0.004	0.004	0.005	0.003	0.006	0.006	0.007	0.004	0.005	0.005	0.006	
Ni	0.003	0.003	0.003	0.004	0.003	0.004	0.003	0.003	0.003	0.003	0.003	0.004	0.003	0.005	0.004	0.004	
Mg	1.904	1.915	1.900	1.904	1.932	1.893	1.904	1.943	1.902	1.902	1.893	1.885	1.923	1.888	1.886	1.944	
Ca	-	-	<0.001	<0.001	-	-	<0.001	-	0.001	<0.001	<0.001	-	<0.001	<0.001	<0.001	-	
Mg#	94.9	95.0	95.1	95.4	97.3	94.2	94.4	97.5	95.1	94.9	94.8	94.0	95.7	94.3	94.9	97.3	
Cat#	3.003	3.008	3.000	2.998	2.993	3.005	3.009	2.997	3.000	3.003	2.999	3.002	3.004	3.001	2.994	2.999	

Alt. Vein = alteration vein (Fig. 7g, late ol)

Normalized to 4 oxygens

Cat# = number of cations

Mg# = (Mg/(Mg + Fe + Ni + Mn))\*100

b.d. below detection limit

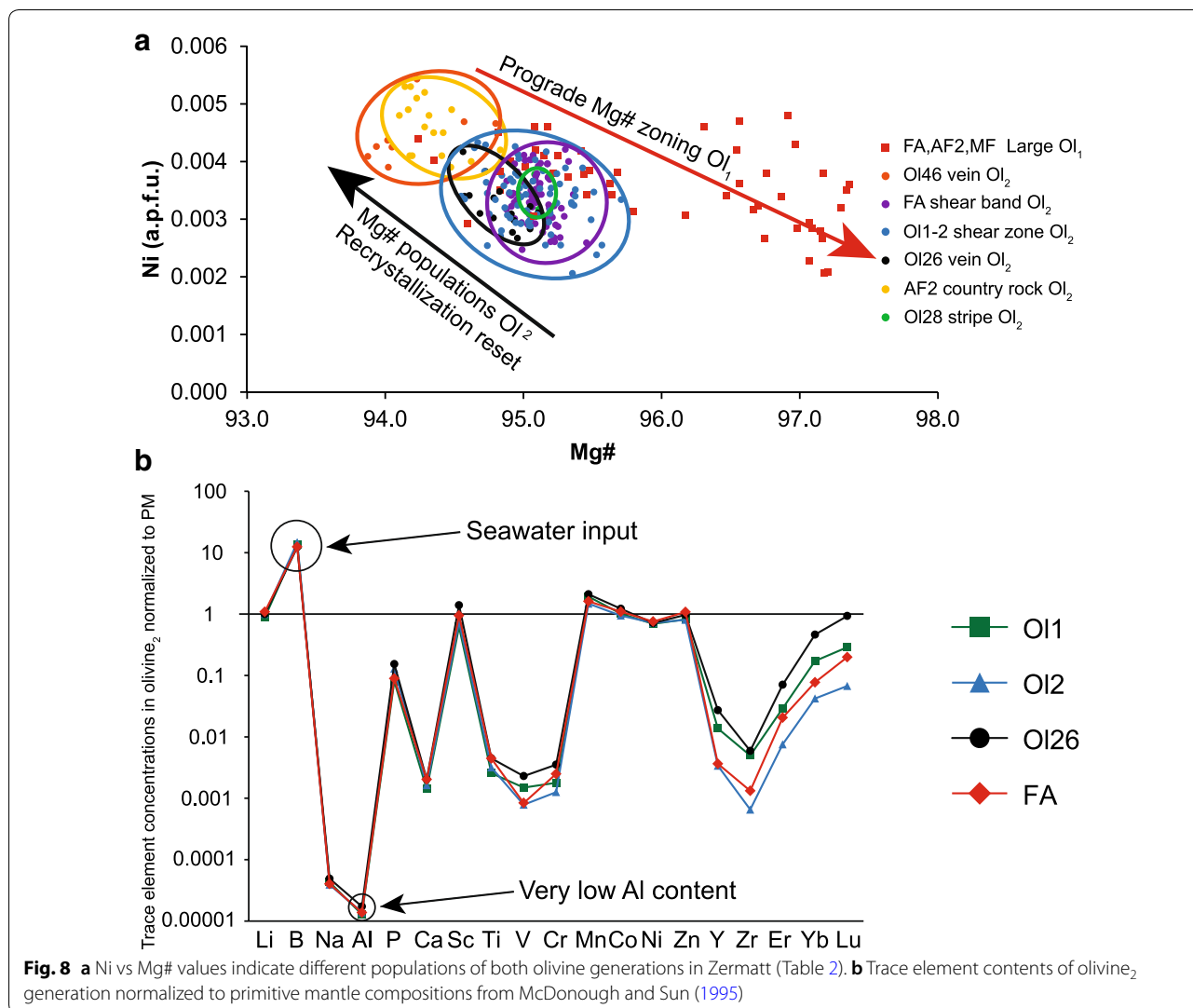


**Table 3** Trace element composition of olivine<sub>2</sub> generation

Samples	<sup>1</sup> n	Li	B	Na	Al	P	Ca	Sc	Ti	V	Cr	Mn	Co	Ni	Zn	Y	Zr	Er	Yb	Lu
Ol1	8	1.41	4.07	0.11	0.30	7.24	35.67	10.04	3.09	0.12	4.69	2008.02	106.61	1356.72	45.17	0.06	0.05	0.01	0.08	0.02
	<sup>2</sup> σ	0.33	0.46	0.05	0.03	1.70	4.16	2.91	0.93	0.08	3.31	117.99	5.07	124.56	2.63	0.02	0.01	<0.01	0.02	0.01
Ol2	8	1.61	4.42	0.10	0.33	11.60	41.24	12.09	3.82	0.06	3.30	1542.24	99.09	1407.91	44.29	0.01	0.01	b.d	0.02	b.d
	σ	0.27	0.62	0.02	0.03	4.66	7.49	2.89	3.41	0.02	1.32	170.70	6.94	187.96	5.29	<0.01	<0.01	-	0.02	-
Ol26	7	1.60	3.69	0.13	0.41	13.83	51.40	22.61	5.39	0.19	9.25	2198.17	128.38	1398.61	53.27	0.12	0.06	0.03	0.20	0.06
	σ	1.30	0.41	0.02	0.02	2.32	6.18	11.63	2.79	0.11	7.73	46.52	3.41	44.47	4.19	0.05	0.01	0.01	0.10	0.03
FA	5	1.74	3.73	0.11	0.32	8.02	51.17	15.38	5.35	0.07	6.53	1684.72	114.92	1479.36	59.33	0.02	0.01	0.01	0.03	0.01
	σ	0.55	0.90	0.04	0.05	2.09	11.12	7.71	2.29	0.03	3.43	38.69	3.08	30.89	4.47	<0.01	<0.01	<0.01	0.01	<0.01

Trace element mass fractions are presented in µg/g

<sup>1</sup>n number of grains analysed, <sup>2</sup>σ standard deviation, b.d. below detection limit

and antigorite form mosaic textures with idioblastic olivine<sub>2</sub>. Antigorite and chlorite contain 2–3 wt% and 10–12 wt% of Al<sub>2</sub>O<sub>3</sub>, respectively (Fig. 10a). The large

olivine shows patchy zoning of randomly distributed cores with Mg# 95, surrounded by rim domains with Mg# 97. The recrystallized, polygonal olivine<sub>2</sub> consists

**Table 4 Major and minor element composition of antigorite and chlorite**

Sample	Antigorite											Chlorite			
	FA						MF		AF2		OI46		FA	OI1	OI46
	p	p	p	p	p	r	p	r	p	r	p	r	p	p	p
SiO <sub>2</sub>	41.89	42.04	41.65	41.92	42.14	43.78	43.01	44.05	42.30	43.62	42.32	43.60	34.35	34.52	33.89
TiO <sub>2</sub>	0.02	0.01	0.02	0.02	b.d.	b.d.	0.02	0.01	b.d.	0.01	0.01	0.01	b.d.	b.d.	b.d.
Al <sub>2</sub> O <sub>3</sub>	2.53	2.59	2.56	2.33	2.77	1.30	2.18	0.78	2.15	1.39	2.58	1.30	11.55	12.59	11.49
Cr <sub>2</sub> O <sub>3</sub>	0.69	0.70	0.76	1.09	0.85	0.08	0.50	0.24	1.70	0.12	0.81	0.20	2.03	0.66	2.64
FeO	2.30	1.95	1.82	1.66	1.90	1.59	2.04	1.33	1.58	1.58	2.06	1.92	2.90	3.10	3.24
MnO	0.03	0.03	0.05	0.03	0.04	0.02	0.04	0.03	0.04	0.01	0.03	0.03	0.04	0.02	0.06
NiO	0.04	0.05	0.01	0.03	b.d.	0.08	0.16	0.06	0.08	0.09	0.03	0.02	0.10	0.07	0.10
MgO	39.53	40.53	40.69	39.94	40.04	40.66	40.33	41.78	39.89	40.58	39.98	40.30	35.92	35.51	35.45
CaO	b.d.	b.d.	0.02	b.d.	0.03	0.01	0.01	b.d.	0.02	0.01	b.d.	0.01	0.05	0.01	0.04
H <sub>2</sub> O	12.02	12.15	12.10	12.04	12.14	12.18	12.22	12.28	12.12	12.16	12.14	12.14	12.65	12.65	12.59
Total	99.05	100.04	99.68	99.06	99.90	99.71	100.53	100.56	99.87	99.59	99.94	99.51	99.58	99.13	99.49
Si	32.395	32.168	31.997	32.362	32.261	33.413	32.716	33.347	32.430	33.339	32.400	33.392	3.257	3.272	3.229
Ti	0.011	0.003	0.012	0.012	–	–	0.010	0.007	–	0.008	0.006	0.004	–	–	–
Al	2.306	2.336	2.318	2.120	2.497	1.169	1.957	0.695	1.943	1.251	2.325	1.170	1.291	1.406	1.290
Cr	0.424	0.424	0.462	0.666	0.514	0.052	0.300	0.141	1.030	0.073	0.489	0.122	0.152	0.050	0.199
Fe <sup>+2</sup>	1.488	1.248	1.170	1.072	1.216	1.012	1.298	0.842	1.013	1.010	1.319	1.229	0.230	0.246	0.258
Mn	0.022	0.021	0.033	0.019	0.026	0.013	0.026	0.022	0.025	0.008	0.019	0.017	0.003	0.001	0.005
Ni	0.025	0.028	0.006	0.019	–	0.047	0.098	0.040	0.049	0.058	0.017	0.010	0.008	0.005	0.008
Mg	45.560	46.220	46.588	45.964	45.695	46.260	45.716	47.137	45.580	46.235	45.612	46.010	5.076	5.017	5.034
Ca	–	–	0.016	–	0.024	0.010	0.005	–	0.013	0.009	–	0.005	0.005	0.001	0.004
H	62.000	62.000	62.000	62.000	62.000	62.000	62.000	62.000	62.000	62.000	62.000	62.000	8.000	8.000	8.000
Mg#	96.7	97.3	97.5	97.6	97.4	97.7	97.0	98.1	97.7	97.7	97.1	97.3	95.5	95.2	94.9
Cat#	82.230	82.449	82.601	82.233	82.233	81.976	82.125	82.229	82.083	81.991	82.187	81.958	10.022	10.001	10.027
Al#	0.29	0.29	0.29	0.26	0.31	0.15	0.24	0.09	0.24	0.16	0.29	0.15			
(Al + Cr)#	0.34	0.35	0.35	0.35	0.38	0.15	0.28	0.10	0.37	0.17	0.35	0.16			

*p* peak metamorphic core, *r* retrograde, *b.d.* below detection limit

Antigorite normalized to 147 oxygens and 62 (OH), Chlorite to 18 oxygens and 8 (OH), total iron as FeO

Cat# = number of cations

Mg# = (Mg/(Mg + Fe + Ni + Mn))\*100

Al# = Al/8, (Al + Cr)# = (Al + Cr)/8, according to Padrón-Navarta et al. (2013)

of cores with lower Mg# 95 and a small rim with Mg# 97 (Fig. 10b). In the mosaic domain, discrete polygonal Ti-clinohumite grains occur in textural equilibrium with olivine<sub>2</sub> (Fig. 10c). On the contrary, Ti-clinohumite occurs as patches or lamellae surrounded by magnetite mesh polygons in the large olivine<sub>1</sub> generation. A detailed map of the well-equilibrated olivine<sub>2</sub> domain shows the mosaic texture between olivine, antigorite and chlorite (Fig. 10e, f). Magnetite in the mosaic domain displays decreasing Cr<sub>2</sub>O<sub>3</sub> contents towards the rim, showing similar chemistry as the relic magnetite mesh polygons in the olivine<sub>1</sub> domain (Fig. 10d). The Al# (Al a.p.f.u./8) indicates the growth of two distinct serpentine generations. The first shows high Al# > 0.3 while the second shows Al# < 0.1.

### 3.4 H<sub>2</sub>O measurements

The two generations of olivine were measured in free-standing thick sections with FTIR spectroscopy in order to determine H<sub>2</sub>O contents of metamorphic olivine. Both olivine generations contain 100–140 µg/g H<sub>2</sub>O, exclusively hosted in Si-vacancies where 4 H replace a Si cation (Kempf & Hermann, 2018). Kempf and Hermann (2018) have shown that this type of defect and the high water contents are diagnostic of olivine formed during the reaction antigorite + brucite = olivine + H<sub>2</sub>O. Additionally, a single H<sub>2</sub>O distribution map has been shown in that work, indicating that no significant H<sub>2</sub>O loss occurred after olivine formation. Here we mapped additional grains from the second generation olivine<sub>2</sub> in sample OI1. Water content maps of olivine<sub>2</sub> display variation between 60 and 180 µg/g H<sub>2</sub>O (Fig. 11). Most of the grains show

**Table 5 Major and minor element composition of Ti-chondrodite and Ti-clinohumite**

Sample	Ti-chondrodite				Ti-clinohumite								
	14			OI1	14		FA	AF2	OI1		MF	OI26	OI46
	l	l	s	s	r	r	p	p	p	p	p	p	p
SiO <sub>2</sub>	32.95	33.14	33.66	33.68	37.48	37.26	37.76	37.39	37.26	37.48	38.53	37.27	37.85
TiO <sub>2</sub>	8.35	9.14	7.61	8.71	3.37	3.72	3.16	2.13	4.88	3.37	2.50	2.98	3.77
Al <sub>2</sub> O <sub>3</sub>	b.d.	0.03	0.01	0.01	b.d.	0.02	b.d.	0.01	0.14	b.d.	0.01	0.03	0.01
Cr <sub>2</sub> O <sub>3</sub>	0.01	0.02	0.01	b.d.	b.d.	b.d.	0.01	0.03	0.01	b.d.	0.01	b.d.	0.01
FeO	7.08	6.23	5.42	3.38	4.81	3.42	3.12	5.35	2.41	4.81	2.40	5.57	4.71
MnO	0.57	0.42	0.42	0.32	0.25	0.39	0.25	0.30	0.28	0.25	0.24	0.32	0.37
NiO	0.09	0.05	0.08	0.09	0.11	0.13	0.14	0.13	0.12	0.11	0.11	0.12	0.11
MgO	47.55	47.29	50.04	50.22	52.37	52.56	53.62	52.44	52.32	52.37	54.25	51.20	52.02
CaO	0.01	0.01	0.03	0.02	b.d.	b.d.	b.d.	b.d.	0.02	b.d.	b.d.	b.d.	0.02
H <sub>2</sub> O <sup>1</sup>	3.13	2.92	3.40	3.11	2.07	1.98	2.13	2.34	1.70	2.07	2.27	2.11	1.97
Total	99.74	99.25	100.72	99.53	100.46	99.49	100.19	100.16	99.14	100.46	100.33	99.65	100.86
Si	1.978	1.997	1.979	1.993	3.981	3.979	3.991	3.981	3.988	3.981	4.053	4.005	4.013
Ti	0.377	0.414	0.336	0.388	0.269	0.299	0.251	0.171	0.393	0.269	0.198	0.241	0.301
Al	–	0.002	0.001	<0.001	–	0.003	–	0.002	0.017	–	0.002	0.003	0.001
Cr	0.001	0.001	<0.001	–	–	–	0.001	0.003	0.001	–	0.001	–	0.001
Fe <sup>+2</sup>	0.355	0.314	0.267	0.167	0.427	0.305	0.276	0.476	0.216	0.427	0.211	0.501	0.418
Mn	0.029	0.022	0.021	0.016	0.022	0.035	0.022	0.027	0.026	0.022	0.022	0.029	0.034
Ni	0.004	0.003	0.004	0.004	0.010	0.012	0.012	0.011	0.010	0.010	0.009	0.010	0.009
Mg	4.255	4.247	4.386	4.430	8.291	8.367	8.447	8.323	8.348	8.291	8.506	8.201	8.221
Ca	<0.001	0.001	0.002	0.001	–	–	–	–	0.002	–	–	–	0.003
H	1.255	1.173	1.334	1.228	1.466	1.407	1.500	1.662	1.217	1.466	1.593	1.515	1.396
Mg#	91.6	92.6	93.8	95.9	94.8	96.0	96.5	94.2	97.1	94.8	97.2	93.8	94.7

Mg# = (Mg/(Mg + Fe + Ni + Mn))\*100

Ti-ch is normalized to 7 cations and 18 charges and Ti-cl on 13 cations and 34 charges

/ large grains (prograde first generation grains), s small grains (recrystallized), p prograde, r retrograde, b.d. below detection limit

<sup>1</sup> H<sub>2</sub>O is recalculated from stoichiometry

zoning unrelated to the principle crystallographic axis of olivine (Fig. 11a, b, f). However, in some grains zoning parallel to the a-axis can be observed (Fig. 11e, see also Kempf and Hermann (2018)). In this olivine (Fig. 11e) there is a gradual decrease from 110 µg/g in the core to 60 µg/g at the rim in a distribution that resembles diffusional loss. However, it is important to note that rim H<sub>2</sub>O mass fractions are still as high (60–100 µg/g) as in grains without any zoning pattern (Fig. 11b). This shows that no significant H<sub>2</sub>O has been lost during exhumation as suggested by Kempf and Hermann (2018). It is more difficult to quantify the H<sub>2</sub>O content of large and inclusion-rich olivine<sub>1</sub> grains. Especially, tiny amounts of hydrous phases such as antigorite and chlorite can provide a large increase of absorbance in the relevant wavenumber region for the Si-vacancy point defect between 3500 and 3650 cm<sup>-1</sup>. In addition, tiny Ti-clinohumite inclusions present as grains or lamellae interfere in the main absorption region of 3500–3600 cm<sup>-1</sup>. This problem was addressed by only measuring the diagnostic 3613 cm<sup>-1</sup>

band in olivine<sub>1</sub> for which there is no interference. From the spectra of clean olivine<sub>2</sub> grains it is evident that the 3613 cm<sup>-1</sup> band contributes 22% to the total absorbance. Thus, multiplying the integrated absorbance of this band in olivine<sub>1</sub> with a conversion coefficient of 4.5, H<sub>2</sub>O contents of 100–110 µg/g are obtained, lying in the same range as olivine<sub>2</sub> grains in the same sample FA 102 µg/g (Additional file 6: Table S4). This provides evidence that olivine<sub>1</sub> and olivine<sub>2</sub> formed at similar high-pressure conditions.

### 3.5 Thermodynamic modelling

All phase diagrams were calculated for a local bulk composition extracted from the compositional map shown in Fig. 10 via XMAPTOOLS (see methods in Lanari and Engi 2017) using the Gibbs free energy minimizer Perple\_X (Connolly 2009), with the thermodynamic dataset of Holland and Powell (1998) revised in 2002 (hp02ver.dat). The extracted bulk composition is MgO: 48.86 wt%, FeO: 3.25%, Al<sub>2</sub>O<sub>3</sub>: 1.66%, SiO<sub>2</sub>: 39.65% (Kempf and

**Table 6 Major and minor element composition of accessory phases**

Sample Mineral	FA		OI26		14		Ilm		inclin Ti-ch		Large ilm		Ilm		Large ilm		OI26		FA		Bc		Bc		FA		Serp		FA		OI26		Cpx		Cpx	
	inclin Cr-Mt	Grt	in vein	Grt	inclin Cr-Mt	Ilm	inclin Ti-ch	Ilm	inclin Ti-ch	Ilm	Large ilm	Large ilm	Ilm	Large ilm	Prv	Bc	Bc	Bc	Prv	Bc	Serp	Cpx	FA	Cpx	FA	Cpx	FA	Cpx								
SiO <sub>2</sub>	35.67		35.90		0.10	0.10	0.07	0.01	0.04	0.04	0.04	0.04	0.04	0.92	b.d.	b.d.	b.d.	0.92	b.d.	41.74	55.64	55.44	55.44	55.64	55.44	55.15	55.15									
TiO <sub>2</sub>	0.56		0.06		58.45	58.13	58.13	56.33	57.93	57.93	57.93	57.93	57.93	53.87	b.d.	b.d.	0.01	0.01	53.87	b.d.	b.d.	b.d.														
Al <sub>2</sub> O <sub>3</sub>	0.16		0.09		b.d.	b.d.	b.d.	0.02	0.01	0.01	0.01	0.01	0.01	b.d.	0.02	b.d.	0.01	0.02	b.d.	0.02	b.d.	0.01	0.01	b.d.	b.d.	0.01	b.d.	b.d.	b.d.							
Cr <sub>2</sub> O <sub>3</sub>	12.15		0.03		0.01	0.01	0.01	0.02	0.01	0.01	0.01	0.01	0.01	b.d.	0.04	0.02	0.04	0.04	b.d.	0.04	0.02	0.02	0.02	0.02	0.02	0.07	0.01	0.01	b.d.	b.d.	0.01	b.d.	b.d.	b.d.		
Fe <sub>2</sub> O <sub>3</sub>	18.26		30.02		6.40	5.89	5.89	6.57	5.17	5.17	5.17	5.17	5.17	–	–	–	–	–	–	–	–	–	–	–	–	–	–	–	–	–	–	–	–	–	–	
FeO	0.48		b.d.		9.16	9.95	9.95	18.64	13.23	13.23	13.23	13.23	13.23	0.67	4.03	4.40	5.92	6.07	0.67	4.03	4.40	5.92	6.07	6.07	6.07	2.29	0.50	0.45	0.45	0.50	0.45	0.36	0.36			
MnO	0.29		b.d.		5.06	5.13	5.13	3.08	3.36	3.36	3.36	3.36	0.11	0.84	0.70	1.09	0.94	0.11	0.84	0.70	1.09	0.94	0.94	0.94	0.16	0.03	0.04	0.04	0.03	0.04	0.03	0.03	0.03	0.03		
NiO	b.d.		b.d.		0.08	0.06	0.06	0.03	0.02	0.02	0.02	0.02	0.01	0.25	0.21	0.24	0.25	0.25	0.01	0.25	0.21	0.24	0.25	0.25	0.19	0.04	0.05	0.05	0.04	0.05	0.02	0.02	0.02	0.02		
MgO	b.d.		0.04		21.50	20.84	20.84	16.17	19.87	19.87	19.87	19.87	0.31	64.80	64.67	62.71	62.70	62.70	0.31	64.80	64.67	62.71	62.70	62.70	62.70	42.80	18.08	17.79	17.79	18.08	17.79	18.04	18.04	18.04		
CaO	33.08		34.59		0.01	0.01	0.01	0.02	0.01	0.01	0.01	0.01	41.31	0.08	0.07	0.07	0.08	0.08	41.31	0.08	0.07	0.07	0.08	0.08	0.06	26.33	26.52	26.52	26.33	26.52	26.65	26.65	26.65			
H <sub>2</sub> O	–		–		–	–	–	–	–	–	–	–	–	30.30	30.27	29.89	29.88	30.30	30.27	29.89	29.88	29.88	29.88	29.88	12.81	–	–	–	–	–	–	–	–			
Total	100.65		100.73		100.76	100.10	100.10	100.90	99.67	99.67	99.67	99.67	97.26	100.38	100.34	99.97	99.96	100.38	100.34	99.97	99.96	99.96	99.96	99.96	100.11	100.64	100.29	100.29	100.64	100.29	100.24	100.24	100.24			
Si	2.981		2.998		0.002	0.002	0.002	<0.001	0.001	0.001	0.001	0.001	0.021	–	–	–	–	0.021	–	–	–	–	–	–	1.953	2.000	2.001	2.001	2.000	2.001	1.993	1.993	1.993			
Ti	0.035		0.004		0.946	0.950	0.950	0.944	0.957	0.957	0.957	0.957	0.932	–	<0.001	<0.001	<0.001	<0.001	0.932	<0.001	<0.001	<0.001	<0.001	<0.001	–	–	–	–	–	–	–	–	–			
Al	0.016		0.009		–	–	–	0.001	<0.001	<0.001	<0.001	<0.001	–	<0.001	–	<0.001	<0.001	–	<0.001	–	<0.001	<0.001	<0.001	<0.001	–	<0.001	–	–	–	–	–	–	–			
Cr	0.803		0.002		<0.001	<0.001	<0.001	<0.001	<0.001	<0.001	<0.001	<0.001	–	<0.001	<0.001	<0.001	<0.001	<0.001	–	<0.001	<0.001	<0.001	<0.001	<0.001	0.003	<0.001	–	–	–	–	–	–	–			
Fe <sup>2+</sup>	0.034		–		0.165	0.181	0.181	0.348	0.243	0.243	0.243	0.243	–	0.033	0.036	0.050	0.051	0.033	0.033	0.036	0.050	0.051	0.051	0.051	0.090	0.015	0.014	0.014	0.015	0.014	0.011	0.011	0.011			
Fe <sup>3+</sup>	1.148		1.887		0.104	0.096	0.096	0.110	0.085	0.085	0.085	0.085	0.013	–	–	–	–	0.013	–	–	–	–	–	–	–	–	–	–	–	–	–	–	–	–		
Mn	0.021		–		0.092	0.094	0.094	0.058	0.063	0.063	0.063	0.063	0.002	0.007	0.006	0.009	0.008	0.002	0.007	0.006	0.009	0.008	0.008	0.008	0.007	0.001	0.001	0.001	0.001	0.001	0.001	0.001	0.001	0.001		
Ni	–		–		0.001	0.001	0.001	0.001	<0.001	<0.001	<0.001	<0.001	<0.001	<0.001	0.002	0.002	0.002	0.002	<0.001	0.002	0.002	0.002	0.002	0.002	0.002	0.007	0.001	0.001	0.001	0.001	0.001	0.001	0.001	0.001		
Mg	–		0.006		0.690	0.675	0.675	0.537	0.650	0.650	0.650	0.650	0.011	0.956	0.955	0.938	0.938	0.011	0.956	0.955	0.938	0.938	0.938	0.938	2.985	0.968	0.957	0.957	0.968	0.957	0.971	0.971	0.971			
Ca	2.962		3.095		<0.001	<0.001	<0.001	<0.001	<0.001	<0.001	<0.001	<0.001	1.018	0.001	0.001	0.001	0.001	1.018	0.001	0.001	0.001	0.001	0.001	0.001	0.003	1.014	1.025	1.025	1.014	1.025	1.032	1.032	1.032			
H	–		–		–	–	–	–	–	–	–	–	–	–	–	–	–	–	–	–	–	–	–	–	–	–	–	–	–	–	–	–	–			
Grossular	<0.001		0.083		0.052	0.048	0.048	0.055	0.043	0.043	0.043	0.043	Mg#	–	2.000	2.000	2.000	2.000	–	2.000	2.000	2.000	2.000	2.000	4.000	–	–	–	–	–	–	–				
Spessartite	0.007		<0.001		0.164	0.181	0.181	0.348	0.243	0.243	0.243	0.243	Cat#	2.000	0.999	1.000	1.000	2.000	0.999	0.999	1.000	1.000	1.000	1.000	96.7	98.3	98.3	98.3	98.3	98.8	98.8	98.8				
Andradite	0.577		0.913		0.689	0.675	0.675	0.538	0.651	0.651	0.651	0.651	–	–	–	–	–	–	–	–	–	–	–	–	–	–	–	–	–	–	–	–	–			
Uvarovite	0.404		0.001		0.092	0.094	0.094	0.058	0.063	0.063	0.063	0.063	–	–	–	–	–	–	–	–	–	–	–	–	–	–	–	–	–	–	–	–	–			

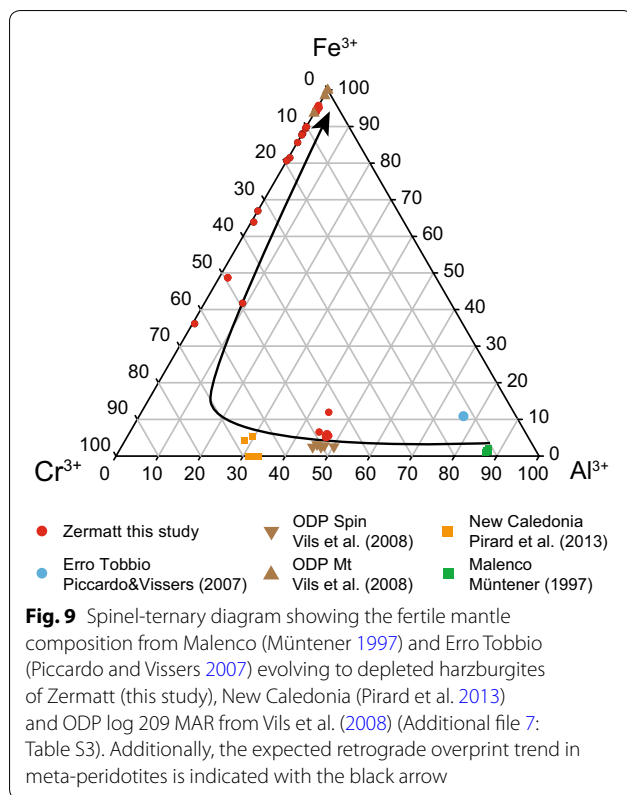
Grt Garnet, Ilm Ilmenite, Prv Perovskite, Bc Brucite, Serp Lizardite/Chrysotile, Cpx clinopyroxene (diopside), b.d. below detection limit

Grt is normalized to 7 cations and 24 charges, Ilm on 2 cations and 6 charges, Prv on 3 oxygens, Bc on 2 oxygens, Serp on 9 oxygens and Cpx on 6 oxygens

Cat# = number of cations

Mg# = (Mg/(Mg + Fe + Ni + Mn))\*100

– Not analysed or calculated



Hermann 2018). Olivine isopleths for Al#, Mg# and wt% were extracted with the *Perple\_X* programme WERAMI. Solution models for olivine, orthopyroxene and brucite were taken from Holland and Powell (1998) and for chlorite from Holland et al. (1998). For antigorite, the aluminium tschermak exchange model of Padrón-Navarta et al. (2013) was used. Figure 12a shows the calculated P–T phase diagram for the local bulk map composition between 1.5 and 3 GPa and 450–700 °C. All assemblages are separated by steep boundaries. Olivine forms from brucite and antigorite first in a ~50 °C broad field where olivine, antigorite and brucite are stable. This olivine is expected to show increasing Mg# 68–92 with increasing temperature where between 0 and 30 wt% olivine is formed. At higher temperatures, chlorite is additionally formed in a narrow field of ~10 °C but 47 wt% olivine is formed in this field for the chosen bulk. At higher temperatures, brucite is exhausted and olivine, antigorite and chlorite coexist over a temperature interval larger than 100 °C. From ~660 °C orthopyroxene appears at first in a very narrow field of a couple of degrees where only 7 more wt% of olivine is formed.

Al# isopleths in antigorite were calculated according to Padrón-Navarta et al. (2013) and displayed in a T–X diagram (Fig. 12b) with variable Al<sub>2</sub>O<sub>3</sub> content ranging from 0 to 3.32 wt% (double the original Al<sub>2</sub>O<sub>3</sub> content)

for 2.5 GPa between 450 and 700 °C (Fig. 12b). The other components of the bulk composition were kept constant. Isoleths of Al# exhibit two major trends. Steep curves indicate no or weak temperature dependence, whereas horizontal lines mean strong temperature dependence. More importantly, fields with horizontal lines contain chlorite while it is absent in fields with steep lines. The Al# in the Ol–Atg–Chl field varies between 0.32 at brucite-out to 0.40 before orthopyroxene-in reactions.

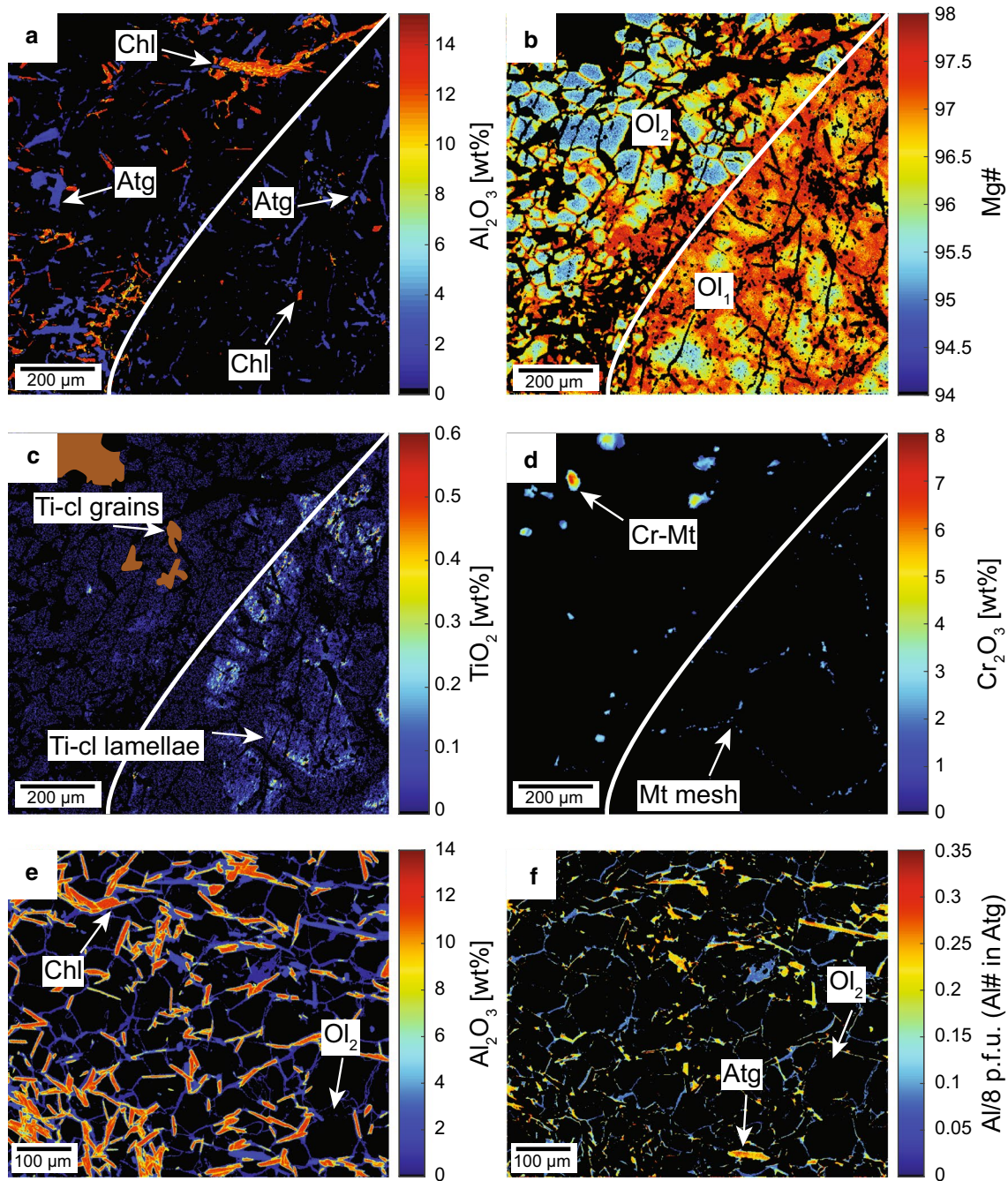
## 4 Discussion

Figure 13 summarizes the main metamorphic stages and associated mineral assemblages that can be deduced from a combination of field observations, thin section petrography and mineral analyses. In the following, we highlight the most relevant features of each stage and show that the serpentinites document a full orogenic cycle from rifting, through seafloor alteration, subduction and finally exhumation. Special emphasis is placed on the formation of brucite during oceanic serpentinization and the consumption of brucite to form metamorphic olivine during subduction. We present different ways of how such metamorphic olivine can be distinguished from mantle olivine. Then we determine the conditions and amounts of fluid that can be liberated by this reaction depending on whether a serpentinized lherzolite, harzburgite or dunite is subducted. Finally, the importance of this reaction for fluid liberation in subduction zones is discussed.

### 4.1 Mantle and oceanic evolution

#### 4.1.1 Mantle relics

The Cr-spinel cores (Fig. 3) are the only relics from the mantle protolith in the serpentinites (Fig. 14). Based on their composition, the Zermatt samples plot in the field of depleted abyssal peridotite. The high Cr# 0.5 indicates a significant melt depletion of ~17% according to Hellebrand et al. (2001) (Fig. 14, Additional file 7: Table S3). This result is consistent with the observation that there are only minor amounts of diopside in the serpentinites, indicating that most clinopyroxene was extracted in the Zermatt-Saas serpentinites during decompression melting (Hirschmann et al. 1998). This is supported with bulk rock data of the serpentinites that display a range in Al<sub>2</sub>O<sub>3</sub> from 0.6 to 2.6 wt%, consistent with a depleted mantle origin (Li et al. 2004b). On the other hand, fertile peridotites are present in the Erro Tobbio, Voltri massive (Piccardo and Vissers 2007) and Malenco peridotites, which plot on the border of the abyssal peridotite array. These samples were described as subcontinental mantle (Müntener and Hermann 1996, 2001; Trommsdorff et al. 1993) showing little melt depletion and very low Cr# in Cr-spinel (Fig. 14). From these observations it is concluded, that the Zermatt-Saas serpentinites derive



**Fig. 10** Quantitative major and minor element maps of a section in sample FA showing the two olivine generations, olivine<sub>1</sub> (Ol<sub>1</sub>) on the right hand side of the white line and olivine<sub>2</sub> (Ol<sub>2</sub>) to the left (**a–d**). The thin section image is given in Additional file 5: Figure S4. **e–f** Quantitative map of a different location within the same thin section FA. **a** Al<sub>2</sub>O<sub>3</sub> content showing the distribution of chlorite and antigorite in both generations. **b** Mg# variation in both olivine generations, note the patchy zoning in olivine<sub>1</sub> versus the apparently concentric zoning in olivine<sub>2</sub>. **c** Ti-clinohumite lamellae in olivine<sub>1</sub> and discrete grains of Ti-clinohumite forming a mosaic texture with olivine<sub>2</sub>. **d** Relic magnetite mesh texture in olivine<sub>1</sub> and relic Cr-rich magnetite in olivine<sub>2</sub>. **e** Al<sub>2</sub>O<sub>3</sub> content of antigorite and chlorite forming a mosaic texture with “black” olivine. **f** Al# indicating two generations of serpentine, high Al# antigorites forming a mosaic texture with chlorite and olivine, note the lower Al# towards their rims, and low Al# serpentine distributed around “black” olivine

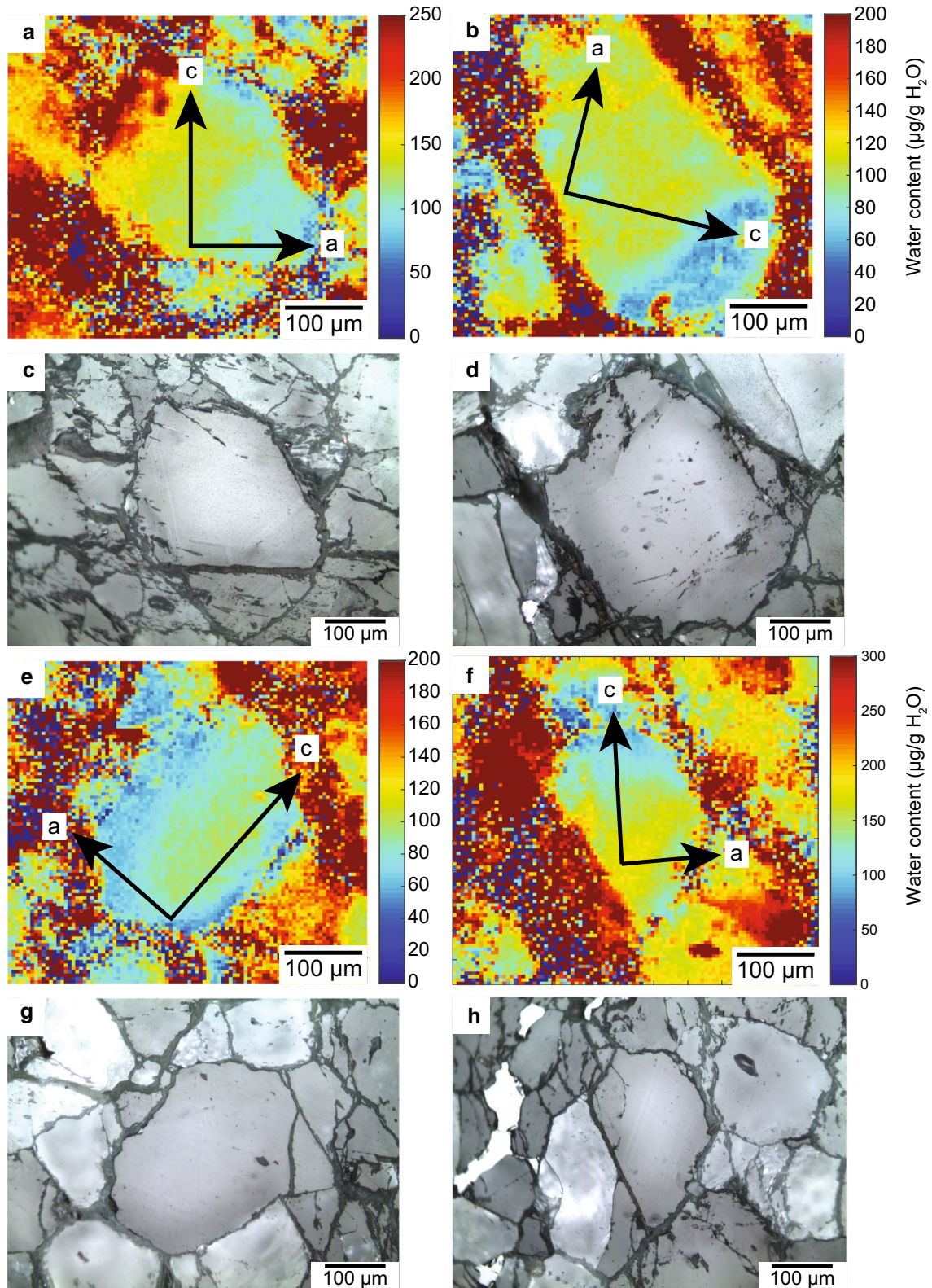
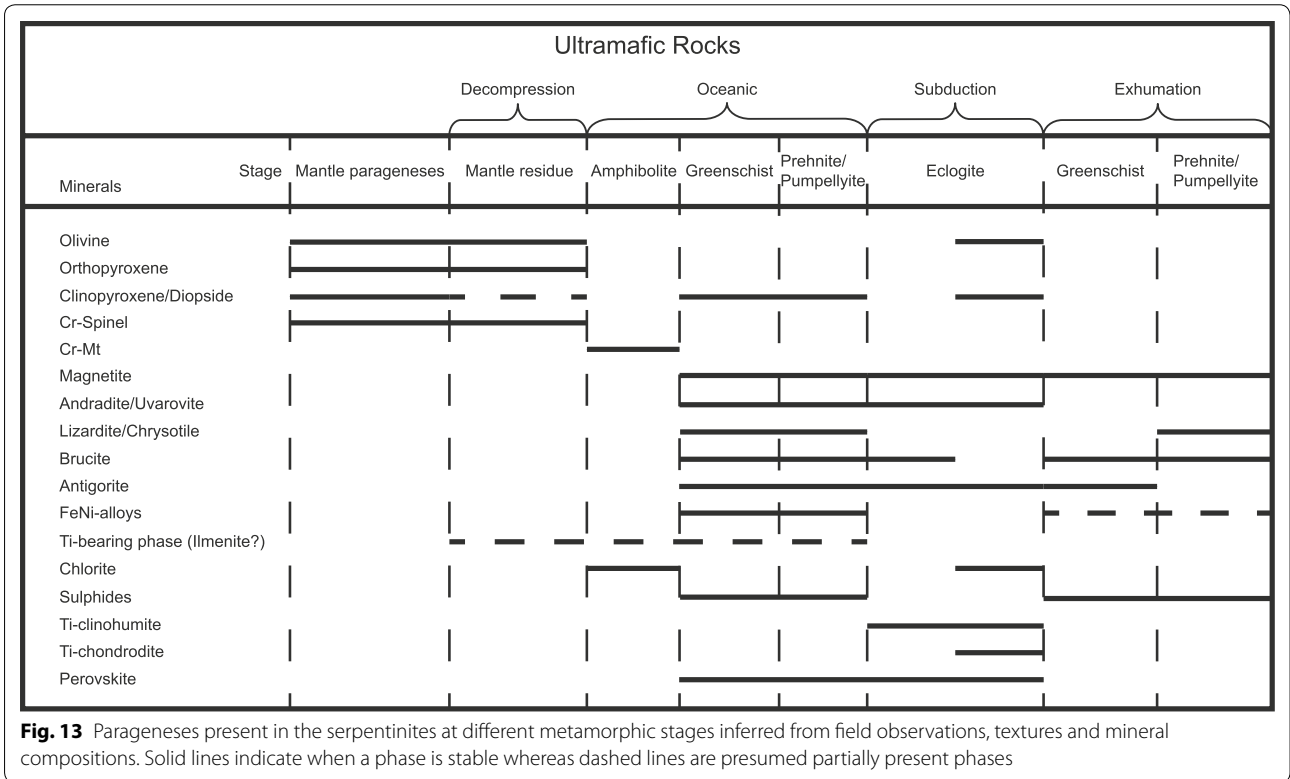
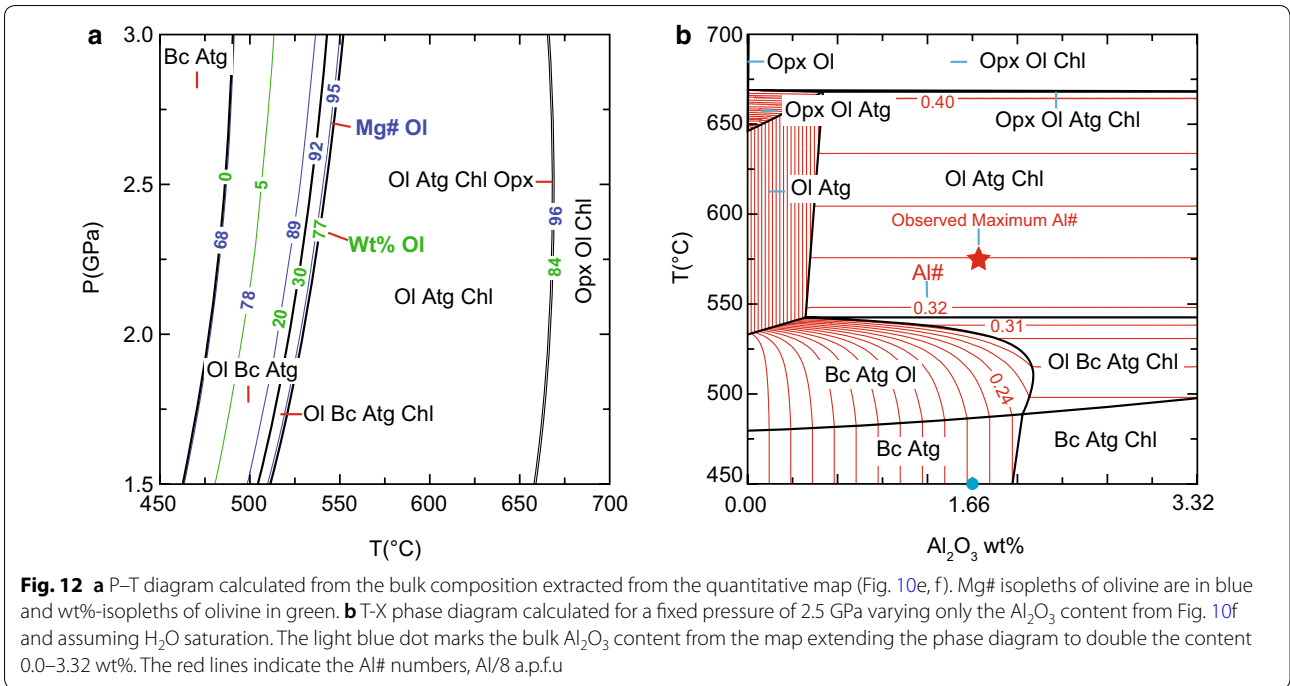
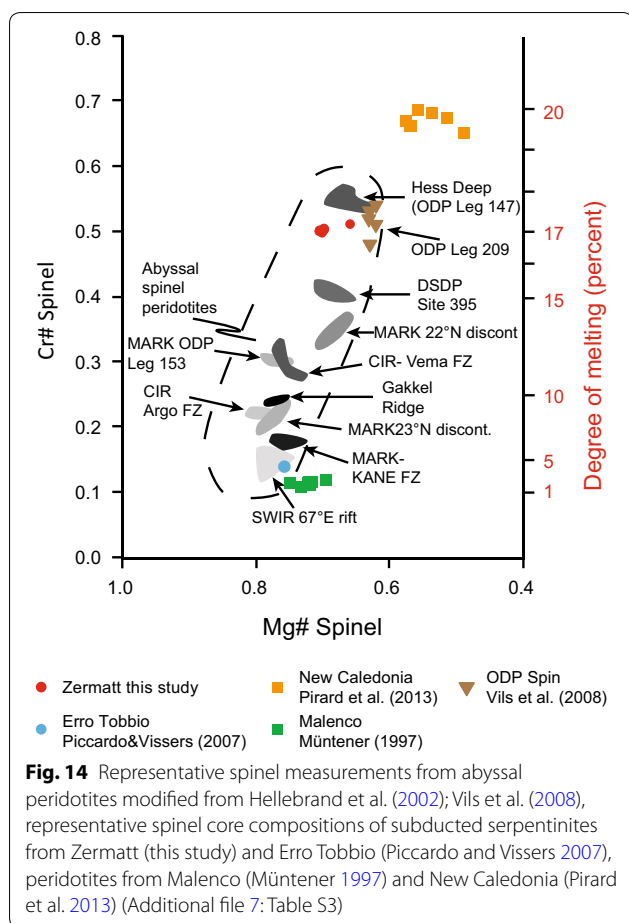


**Fig. 11** H<sub>2</sub>O concentration maps from the shear zone samples OI1-2 in (µg/g) normalized to 1 cm thickness **a, b, e, f** and the corresponding reflected light image **c, d, g, h** respectively. Crystallographic axes are indicated with arrows and boxes. Reflected light images show the grain outlines and the dark rims are late retrograde olivine replacements by lizardite/chrysotile



from a mantle section that might have been closer to an actual spreading centre than the exhumed subcontinental lithospheric mantle sections of Malenco and Erro Tobbio

(Müntener and Hermann 1996; Piccardo et al. 1990; Rampone et al. 2005).



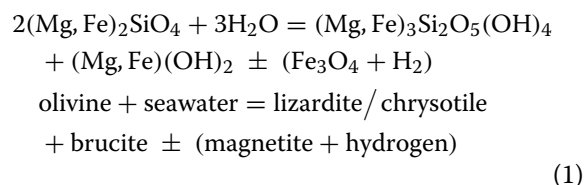
#### 4.1.2 Mafic dykes

The ubiquitous meta-rodingites (Li et al. 2004a) as well as the less frequently observed Ti-chondrodite veins (meta-Ti-gabbro/basalt dykes) provide evidence of melt migration through the former mantle peridotite. Such meta-dykes are commonly interpreted to originate from basalts and Fe–Ti-Gabbro precursors (Gilio et al. 2019; Scambelluri and Rampone 1999; Shen et al. 2014, 2015), respectively, both intruding the local mantle during extension. In the least deformed section of the outcrop, meta-dykes form 90° angles to each other and cut the mantle tectonite foliation. This indicates that the outcropping rocks did not experience any shearing and deformation during the Alpine cycle as any deformation would lead to a lowering of the intersection angle and extensive boudinage of the meta-dykes.

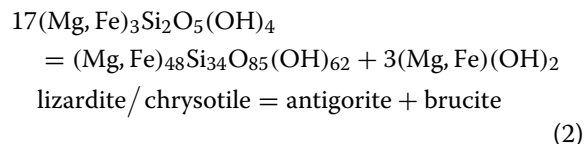
#### 4.1.3 Magnetite and brucite formation during serpentinization

The depleted peridotites were exhumed close to the ocean floor where serpentinization started. During ocean

floor hydration the large relic Cr-spinels from the olivine-serpentinite partially recrystallized to Cr-magnetite rims (Fig. 3) including many sub-micron sized chlorites. Whether a nearly pure oceanic magnetite formed prior to the peak metamorphic rim cannot be inferred but also not excluded due to the presence of the magnetite mesh polygons. The magnetite mesh polygons, if present as inclusions of olivine<sub>1</sub>, are a direct proof for the hydration of mantle olivine. The high modal proportions of magnetite is explained by high temperatures during serpentinization > 325 °C (Klein et al. 2014). Therefore serpentinization might have taken place not directly at the seafloor, but at deeper levels in the oceanic lithosphere. This is in agreement with bulk  $\delta^{18}\text{O}$  values of serpentinites that are in the range of 1.5–4‰, indicative of high temperature serpentinization at 300–400 °C (Cartwright and Barnicoat 1999). Comprehensive serpentinite bulk rock analyses from the same area in Zermatt were presented by Li et al. (2004b) and were shown to be brucite normative because the Si/Mg ratios are lower than pure  $m = 17$  antigorite (Bowen and Tuttle 1949; Coleman and Keith 1971; Hostetler et al. 1966). As FeO is the most important octahedral cation apart from MgO it has an important lever on the amount of brucite versus magnetite production during serpentinization. The more magnetite there is, the less brucite was formed (compare Table 7). Brucite formation occurred during seawater interaction with peridotites. This process has attracted a lot of attention in the literature because of its possible link to early life on Earth (Früh-Green et al. 2004). Studies from IODP samples show the presence of brucite in all studied localities (Bach et al. 2004; Beard et al. 2009; Früh-Green et al. 2004; Kodolányi et al. 2011). The reactions to form brucite, serpentine and magnetite have been thoroughly investigated (Beard et al. 2009; Beard and Frost 2016; Frost and Beard 2007; Klein et al. 2014; Moody 1976; O’Hanley 1996; Schwarzenbach et al. 2016). Accordingly, brucite forms dominantly via the reaction



and in minor amounts from the reaction;



Note that after reaction (2), probably from early stages of subduction, the stable serpentine polymorph

**Table 7 Fluid production from the antigorite + brucite reaction, calculated vs measured**

Bulk rock	Bc in wt % <sup>1</sup>	Bulk H <sub>2</sub> O <sup>1</sup>	T °C <sup>1</sup>	Bulk H <sub>2</sub> O <sup>2</sup>	T °C <sup>2</sup>	Olivine wt % <sup>2</sup>	Fluid wt % <sup>2</sup>	LOI	Mg# Ol <sup>1,2,3</sup>	Mg# Atg <sup>1,2,3</sup>	Mg# Bc <sup>1,2,3</sup>	Mg# Chl <sup>1,2,3</sup>	Mg# Cpx <sup>1,2,3</sup>	Density change <sup>1/2%</sup> <sup>4</sup>
Zermatt														
Lhz*	4.8	11.7	376	8.3	501	22.3	3.4	9.2	26 <sup>1</sup>	93 <sup>1</sup>	93 <sup>1</sup>	98 <sup>1</sup>	84 <sup>1</sup>	2781/2922
									74 <sup>2</sup>	97 <sup>2</sup>	97 <sup>2</sup>	99 <sup>2</sup>	94 <sup>2</sup>	5.1
									95 <sup>3</sup>	93 <sup>3</sup>			98 <sup>3</sup>	
Lhz**	Talc present						No fluid							
Hzb*	6.75	13.2	359	8.4	512	30.8	4.8	11.3	21 <sup>1</sup>	94 <sup>1</sup>	92 <sup>1</sup>			2716/2898
									80 <sup>2</sup>	98 <sup>2</sup>	98 <sup>2</sup>			6.7
Hzb**	1.23	12.5	533	11.7	546	5.1	0.8							2649/2698
														1.8
Dun*	18.3	15.1	309	1.7	530	86.3	13.4	3.6	11 <sup>1</sup>	91 <sup>1</sup>	90 <sup>1</sup>	99 <sup>1</sup>		2696/3257
									89 <sup>2</sup>	98 <sup>2</sup>	98 <sup>2</sup>			20.8
Dun**	12.1	14.6	529	5.5	546	55	11.5							2637/2954
														12
EPMA*	16.8	15.2	480	2.8	543	77.7	12.4	6.3	68 <sup>1</sup>	97 <sup>1</sup>	97 <sup>1</sup>	99 <sup>1</sup>		2636/3129
									95 <sup>2</sup>	99 <sup>2</sup>	99 <sup>2</sup>	95 <sup>2</sup>		18.7
									95 <sup>3</sup>	97 <sup>3</sup>				
EPMA**	14.6	15	533	4.1	551	66.8	8.9							2609/3023
														15.9
Primitive mantle, IODP														
PM*	4.3	11.3	400	8.4	501	19.5	2.9		31 <sup>1</sup>	93 <sup>1</sup>	93 <sup>1</sup>	98 <sup>1</sup>	85 <sup>1</sup>	2795/2922
									74 <sup>2</sup>	97 <sup>2</sup>	97 <sup>2</sup>	99 <sup>2</sup>	94 <sup>2</sup>	4.5
PM**	Talc present													
Hzb*	10.4	13.8	333	6.6	518	47	7.2		15 <sup>1</sup>	91 <sup>1</sup>	91 <sup>1</sup>			2703/2989
									85 <sup>2</sup>	98 <sup>2</sup>	98 <sup>2</sup>			10.6
Hzb**	4.8	13.2	529	9.8	544	20.6	3.4							2637/2772
														5.1
Dun*	13.3	14.2	287	4.8	518	60.8	9.4		8 <sup>1</sup>	90 <sup>1</sup>	89 <sup>1</sup>			2711/3088
									86 <sup>2</sup>	98 <sup>2</sup>	98 <sup>2</sup>			13.9
Dun**	6.7	13.6	529	8.7	530	29.1	4.9							2652/2815
														6.1

Ol-in calculated at 2 GPa, Bc-out at 2.5 GPa

Sources of bulk rock compositions: Zermatt bulk; for phase diagram computation from Li et al. (2004a, 2004b): Lhz = average bulk rock # 16–19 (meta-lherzolites), Hzb = average bulk rock #1–8 & 10–14 (meta-harzburgites), Dun = bulk rock sample lg 15 (meta-dunites)

EPMA bulk from the quantitative map (Fig. 10)

Primitive mantle (PM) from McDonough and Rudnick (1999) (Table 1)

IODP Hzb = average abyssal meta-harzburgites (n = 48), Dun = average abyssal meta-dunites (n = 20): From Deschamps et al. (2013) (Table 1)

1. LOI's [wt% H<sub>2</sub>O] from Li et al. (2004a, 2004b). 2. As soon as talc is present brucite is absent

\* All iron as FeO = FeO<sub>tot</sub>

\*\* Bulk – FeO<sub>tot</sub>

<sup>1</sup> Calculated at Ol-in [wt% H<sub>2</sub>O]

<sup>2</sup> Calculated at Bc-out [wt% H<sub>2</sub>O]

<sup>3</sup> Natural olivines at Bc-out Measured with EPMA

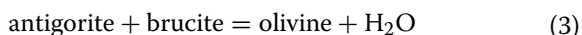
<sup>4</sup> Density change in kg/m<sup>3</sup> and in mass%

is antigorite. The Mg# of brucite is expected to be lower than that of the mantle olivine while the one for lizardite is expected to be higher. From the iron-rich brucite, secondary magnetite can form through oxidation which decreases the amount of brucite and increases its Mg# (Bach et al. 2006; Beard and Frost 2016). O'Hanley and Dyar (1993) have shown that lizardite can incorporate more Fe<sup>3+</sup> than antigorite. Therefore, at the transition of lizardite to antigorite, additional magnetite might have formed. Redistribution of SiO<sub>2</sub> during serpentinization from sediments and seawater will consume brucite. IODP samples mostly originate from the uppermost hundreds of meters in an oceanic crust and have a limited access to the deeper levels where fluids and sediments have a decreasing potential to influence serpentinization. Modal brucite formation during serpentinization is dependent on the degree of melt depletion of the primitive mantle, showing increasing modal olivine content (and thus decreasing Si/Mg) with increasing depletion, mainly due to pyroxene extraction. The extent of brucite formation in the variably depleted oceanic mantle is then linked to the degree of serpentinization of the oceanic crust at depth. The degree of serpentinization is important since olivine is the first phase to serpentinize while orthopyroxene is more stable and thus relatively more brucite is formed at depth (Schwarzenbach et al. 2016).

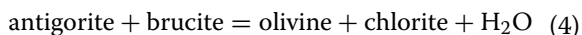
## 4.2 Prograde metamorphic olivine growth

### 4.2.1 Phase analysis

There are not many metamorphic reactions that allow the construction of detailed prograde P–T paths in serpentinites. Reaction 2 roughly coincides with the transition from sub-greenschist to greenschist facies (Evans 2004; Trommsdorff and Evans 1974). Then, the antigorite + brucite reaction provides an important marker to distinguish between greenschist/blueschist facies conditions (olivine free) and epidote–amphibolite/eclogite facies conditions where metamorphic olivine is present. The MgO–SiO<sub>2</sub>–H<sub>2</sub>O is the simplest chemical system where forsterite is formed along an univariant reaction:



With the additional component Al<sub>2</sub>O<sub>3</sub> present in antigorite as Al-Tschemak a new phase needs to form on the product side of the equation which is chlorite:



Adding ferrous iron to the system transforms univariant lines into divariant fields. Based on a reactive

bulk composition extracted from compositional maps (Fig. 10e, f), olivine formation is predicted to occur within ~50 °C where antigorite, brucite and olivine are stable and additionally in a narrow ~10 °C field towards higher temperatures where chlorite is formed (Fig. 12a). The erratic distribution of lower Mg# patches (Fig. 10b) in olivine<sub>1</sub> is explained by Fe–Mg-mixing properties of the olivine solid solution where Fe-rich olivine becomes progressively more Mg-rich with increasing temperature seen in the blue Mg# isopleths in Fig. 12a. For metamorphic olivine formed during serpentinite subduction this behaviour was studied by Kunugiza (1982) in the Sanbagawa metamorphic belt and is equivalent for the formation of the olivine<sub>1</sub> generation.

### 4.2.2 Olivine zoning

Olivine<sub>1</sub> growth started forming more iron-rich patches with Mg# 95 first, becoming increasingly MgO-enriched towards rims (Mg# 97) (Figs. 8a, 10b). The distribution of the lower Mg# 95 nuclei may be governed by the initial distribution of FeO in the reactant minerals antigorite and brucite. The overall very high Mg# is related to the high amount of magnetite in the sample that sequesters a significant proportion of the Fe in the bulk rock. The lower average Mg# 94–95 of olivine<sub>2</sub> (Fig. 10b), that clearly originates from recrystallization of olivine<sub>1</sub>, is not in agreement with the expected Mg# increase at higher temperatures (Fig. 12a). A possible explanation is the consumption of the magnetite mesh polygons as observed (Figs. 5b–d). This requires either Fe<sup>3+</sup> to be reduced to Fe<sup>2+</sup> in order to be incorporated by olivine or while ferrous iron is incorporated in olivine ferric iron is hosted in coexisting minerals. There are several possibilities how this could be achieved. (1) The simplest explanation is that magnetite reacted with relic alloys to form a FeO component that was incorporated into olivine. The presence of andradite-uvarovite garnet with magnetite (Mt) and occasionally with diopside and or chlorite in sample FA (Fig. 4g) and olivine veins Ol26 (Fig. 6f, g) suggests the former presence of metal alloys such as taenite-awaruite at the ocean floor stage (Frost 1985). The absence of FeNi-alloys in the prograde assemblage suggests their participation in the olivine forming reactions. (2) A second hypothesis is that magnetite reacted with sulphides releasing Fe<sup>2+</sup>, while the sulphides were oxidised (Merkulova et al. 2017). The produced SO<sub>2</sub> would then be able to leave the system with the water-rich fluid. However, a recent study has shown, that the fO<sub>2</sub> for the antigorite + brucite to olivine reaction is well below QFM and that SO<sub>2</sub> is only present in trace amounts in the fluid

at the corresponding P–T conditions (Piccoli et al. 2019). (3) While the FeO component of magnetite is incorporated into olivine, some MgO of olivine is incorporated into magnetite and the ferric iron (or Cr in the case of Cr-magnetite) might be accommodated by existing or newly formed phases. For example, the high Cr-contents in both peak metamorphic antigorite and chlorite (Table 4) can be explained by the consumption of magnetite and Cr-magnetite that contain 4 wt% and 46 wt% Cr<sub>2</sub>O<sub>3</sub>, respectively. Another possibility is that new andradite garnet is formed hosting the ferric iron liberated by magnetite breakdown. In any case, magnetite does not seem to be fully inert during the olivine forming reaction. Also, two possibilities are suggested for sulphide participation due to the observed scarcity of sulphides in the olivine<sub>2</sub> domain. (1) They partially re-equilibrated where their iron component (ferrous) partitioned into olivine while their Ni-content passively increased in sulphides, thereby decreasing the volume of sulphides present. (2) At the low oxygen fugacity, sulphur might be lost as H<sub>2</sub>S (Piccoli et al. 2019) decreasing the amount of sulphides and making Ni and Fe available for olivine. Considering thermodynamic equilibrium, it is unlikely that the sulphides remained inert during the olivine forming reaction.

#### 4.2.3 Al-in-antigorite and olivine

The Al# isopleths for antigorite show the temperature dependence of the tschermak exchange in antigorite once its Al content is buffered by an Al-rich phase (Padrón-Navarta et al. 2013). This is achieved when chlorite becomes stable. The maximum Al# from the map is 0.32 (Fig. 10f), in line with the modelled maximum values from Fig. 12b. This indicates a minimum temperature of 520 °C at a pressure of 1.5 GPa and a maximum temperature of 560 °C at a pressure of 3.0 GPa. Moreover, Padrón-Navarta et al. (2013) discussed the influence of elevated Cr<sub>2</sub>O<sub>3</sub> mass fractions in natural antigorite on the Tschermak substitution thermometer which was calibrated on 0.21–0.34 a.p.f.u. Cr contents. Because, peak antigorite (Table 4) in Zermatt attains up to 1.03 a.p.f.u. Cr producing (Al + Cr)# 0.34–0.38. This suggests ~30–60 °C higher peak temperatures than calculated here. Trace element measurements showed that metamorphic olivine contains 0.3–0.41 µg/g Al. Applying the pure Al-in-olivine thermometer (without Cr) returns temperatures between 575–590 ± 20 °C (De Hoog et al. 2010), in excellent agreement with the other determinations. Therefore, the maximum temperature of peak metamorphism is closer to the antigorite + brucite reaction rather than the antigorite-out reaction as suggested in other works (Bucher and Grapes 2009; Zannoni et al. 2016) and also supported by the absence of orthopyroxene in the area. On the other

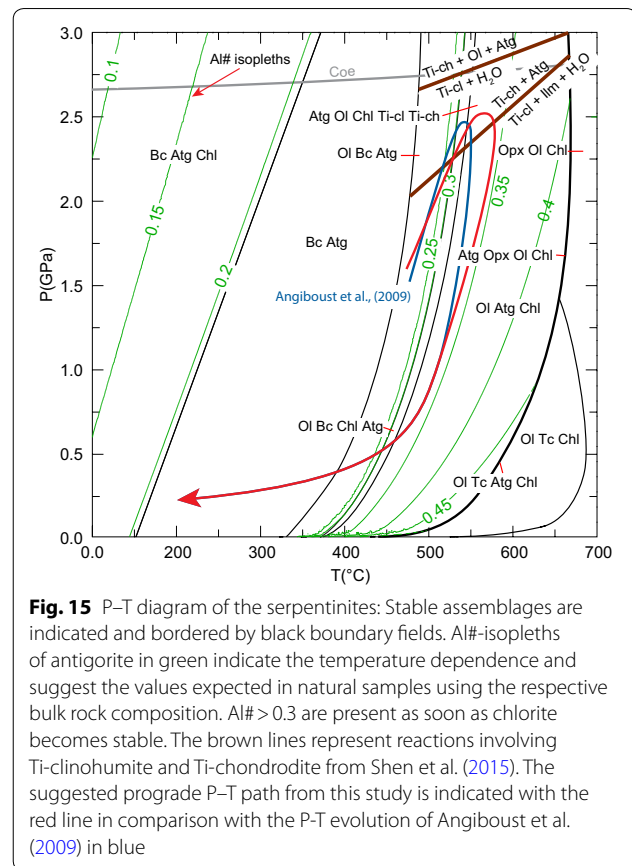


**Fig. 15** P–T diagram of the serpentinites: Stable assemblages are indicated and bordered by black boundary fields. Al#-isopleths of antigorite in green indicate the temperature dependence and suggest the values expected in natural samples using the respective bulk rock composition. Al# > 0.3 are present as soon as chlorite becomes stable. The brown lines represent reactions involving Ti-clinohumite and Ti-chondrodite from Shen et al. (2015). The suggested prograde P–T path from this study is indicated with the red line in comparison with the P–T evolution of Angiboust et al. (2009) in blue

hand, peak temperatures as low as 500 °C suggested by Weber and Bucher (2015) can also be excluded due to the observed mineral assemblage.

A word of caution is required for the application of Al-in-antigorite as a thermometer. Figure 10f shows the second serpentine generation growing around polygonal olivine grains. Their very low Al# clearly separates them from peak antigorite whose Al content is diluted at rims. The dilution of the Al# indicates partial re-equilibration with late serpentine and is likely experienced when measuring antigorite in spot analyses mode with EPMA i.e., instead of obtaining Al# 0.32 as in Fig. 10f a lower value of Al# 0.29–0.31 is obtained in all samples (Table 4). Peak temperatures are thus prone to being underestimated. On the other hand, the lower values are also generated by overlap measurements over the zoned antigorite blades owing to the necessary beam diameter spreading during EPMA measurements. This is commonly done to avoid beam damage in the measured serpentine grains. Furthermore, this clearly shows the value of the mapping technique even though high currents are used, calibration with spot analyses guarantees the link between X-ray intensity and composition.

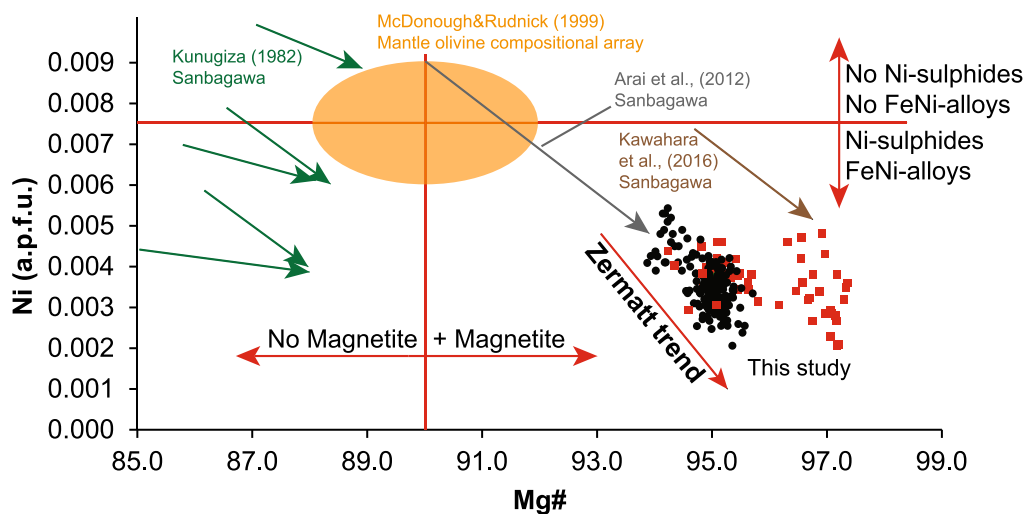
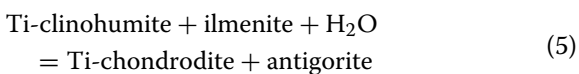


**Fig. 16** Ni vs Mg# trends in prograde metamorphic olivine in Zermatt samples, red symbols olivine<sub>1</sub> and black symbols olivine<sub>2</sub> (data from Fig. 8a and Additional file 3: Table S2), compared with the Sanbagawa metamorphic belt in Japan (Arai et al. 2012; Kawahara et al. 2016; Kunugiza 1982) (core to rim trends indicated with arrows). The orange field indicates the mantle array of Ni (a.p.f.u.) vs Mg# (McDonough and Rudnick 1999). Red lines show the controls of magnetite, FeNi-alloys and sulphide presence on olivine compositions that derive from the antigorite + brucite reaction

#### 4.2.4 Pressure constraints

Pressure constraints can be deduced from the Ti-clinohumite/Ti-chondrodite equilibria (Shen et al. (2015) in the shear zone and in the Ti-Chondrodite vein (Fig. 15). Ti-chondrodite can be formed through the reaction:



This indicates that once the Ti content in Ti-clinohumite is buffered, Ti-chondrodite forms at the expense of Ti-clinohumite between 480 °C and 2.0 GPa and 660 °C and 2.8 GPa. However, at higher pressures, Ti-clinohumite disappears along



between 490 °C and 2.6 GPa and 670 °C and 3.0 GPa. Ti-clinohumite is present as minute lamellae dispersed within the large olivine<sub>1</sub> as well as polygonal grains within the recrystallized olivine<sub>2</sub> (Fig. 10c). Ti-chondrodite coexists with Ti-clinohumite and is abundant in the Ti-rich veins, where precursor ilmenite must have been present. Most grains present in the shear zone, shear bands and olivine veins consist of Ti-clinohumite. A single Ti-chondrodite grain was observed in the shear zone (sample Ol1-2). This grain is strongly retrogressed to Ti-poor magnetite and Ti-clinohumite but no ilmenite is present, suggesting a possible Ti-chondrodite formation via

reaction (6). However, the shear zone is juxtaposed to a metarodingite generally enriched in Ti. The key observation is that olivine, Ti-chondrodite and Ti-clinohumite coexist, which provides a good constraint for pressure when coupled with the tschermak model for antigorite and Al-in-olivine thermometry. For the peak temperature of 570–590 °C, the pressure range where Ti-chondrodite and Ti-clinohumite coexist is between 2.3 and 2.9 GPa.

Ti-chondrodite has been described in the Zermatt-Saas serpentinites to the south in the Valtournanche valley, Italy. A possible UHP origin of these serpentinites was suggested by Luoni et al. (2018). However, Ti-chondrodite is generally associated to Ti-rich lithologies (see their Appendix) and coexists with Ti-clinohumite. Ti-chondrodite also occurs in veins in serpentinites close to the UHP unit of Lago di Cignana, but also there it derives from former Ti-rich mafic dykes (Gilio et al. 2019).

### 4.3 Comparison with other rocks

#### 4.3.1 Peak conditions

Published peak temperatures and pressures of 550–600 °C and 2.5–3.0 GPa in nearby eclogites (Bucher et al. 2005), between 600 and 610 °C and 2.5 GPa in metabasites (Bucher and Grapes 2009) are in good agreement with our thermobarometric data. The lower end of these pressure estimates is preferred due to the absence of coesite (Coe) in the meta-mafic and meta-sedimentary rocks of the ophiolite sequence (see Fig. 15). We derive from the combined evidence that olivine formation

occurred close to peak P–T conditions on the prograde path through the involvement of brucite at temperatures of 550–600 °C and pressures >2.0 GPa but <2.7 GPa (Fig. 15). A comprehensive overview of P–T estimates for the whole Zermatt-Saas zone eclogites is provided by Angiboust et al. (2009). Their estimates of  $540 \pm 20$  °C and  $2.3 \pm 0.1$  GPa are in excellent agreement with our peak metamorphic conditions. Similar estimates,  $500 \pm 50$  °C and  $2.2 \pm 0.2$  GPa (de Meyer et al. 2014), were reported from the metasedimentary cover of the Zermatt-Saas ophiolite at Triftji (Fig. 1) that is surrounded by the olivine-bearing serpentinites described in this study.

Bucher et al. (2005) suggested that the eclogites at Pfulwe formed through external fluids from serpentine breakdown. Bucher and Grapes (2009) showed that over 90% of the eclogite facies peak parageneses in the Allalingabbro formed due to large amounts of external fluids at the peak P–T as did Li et al. (2008) in the eclogites facies metarodingites throughout the Zermatt-Saas serpentinites. As shown here antigorite breakdown conditions were never attained. The determined P–T of eclogite transformation coincides well with the peak P–T estimates of the antigorite + brucite reaction presented here. Thus, the good overall agreement between P–T estimates from ultramafic, mafic and sedimentary rocks shows that all rocks equilibrated close to peak metamorphic conditions possibly triggered by the large amount of fluid released by the antigorite + brucite reaction.

#### 4.3.2 Retrograde path

The presence of fluids during exhumation is documented by talc-carbonate veins since they crosscut the prograde olivine-serpentine (Fig. 7a). Additionally, antigorite veins pseudomorphically replace metamorphic olivine which indicates the presence of Si-bearing fluids due to the absence of brucite (Fig. 7b, c). Both assemblages of these veins could have formed anywhere on the retrograde path after olivine formation. An important constraint from the serpentinites is that the exhumation path does not cross the talc + olivine field meaning that a low-pressure antigorite-breakdown has not occurred (Fig. 15). Greenschist facies overprint at 0.4–0.6 GPa and 400–450 °C in the meta-mafic rocks was described in several studies (Bearth 1967; Bucher et al. 2005; Cartwright and Barnicoat 2002; de Meyer et al. 2014; Reinecke 1991; Rubatto et al. 1998). The nearly isothermal decompression (fast exhumation path) in the area suggested by many studies (Agard et al. 2009; Cartwright and Barnicoat 2002; de Meyer et al. 2014; Reinecke 1991; Rubatto et al. 1998) is in line with our observations.

## 4.4 Metamorphic olivine derived from the antigorite + brucite reaction

### 4.4.1 Textures, major, minor and trace elements

Recognition of metamorphic olivine formed from antigorite + brucite is challenging since it is variably abundant throughout serpentinites in the field and is often strongly overprinted. For example, most serpentinites involved in subduction, exhumation and obduction are strongly sheared. Pre-alpine textures are thus often smeared out and retrograde overprint partially re-serpentinizes metamorphic olivine with and without brucite formation (Fig. 7). Recognizing metamorphic olivine is important as it provides a documentation of fluid-producing reactions during subduction. The following set of tools can be used to distinguish metamorphic olivine of the antigorite + brucite reaction from mantle olivine.

The olivine<sub>1</sub> generation clearly overgrows magnetite polygons (Figs. 5b, 10d) typically representing the mesh texture and magnetite veins formed during ocean floor hydration of mantle olivine (O'Hanley 1996; Wicks and Whittaker 1977). The presence of Ti-clinohumite lamellae (clearly a metamorphic mineral) in olivine<sub>1</sub>, in the core of the magnetite polygons, (Fig. 10c) indicates metamorphic growth of olivine. From the major element composition, the very high Mg# 95–97 (Fig. 10b) is explained by the coexistence with Cr-magnetite and magnetite and deviates significantly from the compositional array of upper mantle olivine (Mg# 88–92, see Fig. 16). NiO in metamorphic olivine (0.11–0.27 wt%) is generally lower than in mantle olivine (0.4 wt%; reported in McDonough and Rudnick (1999) whereas MnO shows elevated concentrations (0.16–0.36 wt%) compared to mantle olivine (0.14 wt%). Various studies on metamorphic olivine in the Sanbagawa belt in Japan found comparable core-rim trends (Arai et al. 2012; Kawahara et al. 2016; Kunugiza 1982) to what is observed in our study (Fig. 16). The lower NiO content is due to the presence of Ni-sulphides (pentlandite e.g. Piccoli et al. 2019), the large amount of magnetite and the former presence of FeNi-alloys (taenite-awaruite). The elevated MnO in olivine points to a co-existence with antigorite that has MnO contents below 0.05 wt%. A typical trace element marker for metamorphic olivine from dehydration reactions in oceanic lithosphere is B, since it is enriched in seawater (Scambelluri et al. 2001, 2004; Seyfried and Dibble 1984; Tenthorey and Hermann 2004; Thompson and Melson 1970; Vils 2009; Vils et al. 2011, 2008). However, to our knowledge, there is currently no comprehensive study of B systematics in pristine mantle olivine except for a couple of analyses on Kimberlites (Kent and Rossman 2002). Therefore, all data were normalized to primitive mantle compositions from McDonough and Sun (1995). The greater

than tenfold enrichment of B relative to primitive mantle values (8b and Table 3) is a further clear indicator for a seawater signature (Kodolányi et al. 2011). Additionally, most trace element contents are lower than primitive mantle olivine values. Another good example is Al that has been used as a thermometer in peridotites (De Hoog et al. 2010). Equilibration temperatures of 800–1400 °C result in highly variable Al contents of 10–800 µg/g Al. The lower formation temperatures of olivine from the antigorite + brucite reaction leads to distinctly lower Al contents of 0.3–0.41 µg/g. Therefore, textural and compositional data can help for the identification of olivine that grew from the antigorite + brucite reaction.

#### 4.4.2 Water in olivine

Hydrogen incorporated into Si-vacancies conveniently measured with FTIR spectroscopy is another very strong indicator for the presence of brucite during olivine formation. The antigorite + brucite reaction (4) produces H<sub>2</sub>O and thus favours a high water activity in the free fluid phase. At the same time the assemblage in the divariant field antigorite-brucite-chlorite-olivine imposes a low SiO<sub>2</sub> activity such that Si-vacancies form in the product olivine (Kempf and Hermann 2018). The mapped H<sub>2</sub>O distribution in randomly oriented olivine grains displays no systematic relationships with the crystallographic axis (Fig. 11). There is no sign of a normal tracer diffusional loss of H<sub>2</sub>O. Even if a few grains display concentric zoning, H<sub>2</sub>O mass fractions never go to zero at rims and can thus be interpreted as growth zoning (Kempf and Hermann 2018). Water contents in the olivine<sub>2</sub> (sample Oll-2, shear zone) generation presented in the maps are well above 100 µg/g in agreement with the values provided by Kempf and Hermann (2018). The water contents of the inclusion-rich, large olivine<sub>1</sub> generation, are within uncertainty identical with olivine<sub>2</sub>. The core-rim contents can vary by > 50%, generally decreasing towards the rims. FTIR spectra of olivine<sub>1</sub> also display absorption at 3370–3400 cm<sup>-1</sup>, which is typical for Ti-clinohumite lamellae (Shen et al. 2014) and thus a metamorphic origin of the olivine.

The combined evidence from textures, composition and FTIR spectroscopy demonstrates that all olivine in the serpentinite has grown from the antigorite + brucite reaction on the prograde path. This contradicts previous studies that suggested that such olivine represents recrystallized mantle olivine (Li et al. 2004b; Rahn and Rahn 1998).

#### 4.4.3 Metamorphic olivine as a proxy for brucite distribution in the field

It is notoriously difficult in lower grade serpentinites to detect brucite due to its small grain size and the tendency to intergrow with serpentine minerals. As we have established, that all the olivine in the mapped outcrop derives from the antigorite + brucite reaction, we can now use the distribution of olivine to infer the former distribution of brucite. In the least deformed part of the serpentinite there is a pronounced stripe pattern at the 10–20-cm scale consisting of olivine-bearing dark versus the olivine-absent green serpentinites, providing evidence for a heterogeneous brucite distribution at the mesoscale (Fig. 3a). In other undeformed areas, olivine occurs in patches that are distributed more evenly throughout the rock (Fig. 5a). A significant proportion of the outcrop does not contain olivine at all, indicating that these parts may derive from a brucite-free protolith. As discussed above, the formation of brucite during ocean floor alteration depends on many factors including variation in bulk Si/Mg as well as changing formation conditions. The eclogite-facies olivine bearing serpentinite might thus still document major alteration processes that occurred at the ocean floor. More detailed studies, especially including oxygen isotopes, are needed to fully exploit this information.

#### 4.4.4 Olivine as marker for fluid pathways in subducted serpentinites

The antigorite + brucite reaction produces 30 wt% of olivine<sub>1</sub> and a total of 77 wt% olivine<sub>1</sub> and olivine<sub>2</sub> according to the calculated model shown in Fig. 12a at reactions (3, 4), leading to a significant change in density and volume of the involved serpentinite for this olivine-rich local bulk rock composition (Table 7). This allows fluid to be pooled first at grain boundaries (Fig. 5d) in agreement with the model of Plümper et al. (2017). The fluid produced is subsequently flowing along grain boundaries and thought to form small fluid conduits visible as shear bands in the field gathering into broader shear zones (Fig. 6a, b, e) and olivine veins (Fig. 6d) as also supported by the focused fluid flow model of Plümper et al. (2017). Therefore, in the more deformed parts of the outcrop, the distribution of metamorphic olivine can be used to trace the pathways of the escaping fluid from reactions (3, 4). Olivine veins are often aligned en-echelon along the shear zones, providing evidence for synkinematic precipitation of olivine in veins with movements along the shear zones. The exact link between this fluid release and the mylonite formation is not yet clear. Nevertheless, the significant fluid release and associated volume decrease (Table 7) in shear zones would be large enough

to potentially trigger deep earthquakes. The fluid passes also through metarodingites where it dissolves diopside, andradite and perovskite and precipitates them in olivine veins (Fig. 6d). How far certain elements are able to travel within this vein-shear zone system requires also further investigation.

#### 4.4.5 Implications of hydrous olivine on slab rheology and the deep water cycle

Olivine-rich rocks such as olivine veins, shear zones and olivine-rich meta-harzburgites produced by the antigorite + brucite reaction are more competent than the neighbouring serpentinites. However, this relationship might change after the breakdown of chlorite and antigorite during further subduction. The olivine derived from the antigorite + brucite reaction contains up to 10 times more H<sub>2</sub>O than what is expected at the antigorite-out reaction and about 4 times more water than at the chlorite-out reaction (Padrón-Navarta and Hermann 2017). H replacing Si has a strong influence on the rheology of olivine-dominated rocks (Faul et al. 2016). Therefore olivine-rich shear zones that derive from the antigorite + brucite reaction might be weaker than the later produced olivine from antigorite- and chlorite-breakdown and play an important role for strain localisation within the slab. This hypothesis is based on the assumption that there is no diffusional equilibration of H in Si-vacancies in olivine with further subduction. A recent experimental study on the Zermatt olivines (sample Oll-2) from this outcrop by Jollands et al. (2019) has shown that at atmospheric pressures the Si-vacancies are dehydrogenated within hours at elevated temperatures. However, the study also showed that dehydrogenation in 1 atm experiments is not easily extrapolated to natural conditions and that H loss or gain is governed by a complex interplay of inter-site reactions and diffusion.

#### 4.5 Modelled vs. observed mineral compositions: The temperature interval of fluid release

A close inspection of the phase diagram results (Fig. 12a) suggests that the first olivine nucleus should show Mg# as low as 68 at the olivine-in reaction, which is significantly lower than the observed Mg# 95 crystallization centres of olivine<sub>1</sub> (compare Fig. 10b with Fig. 12a). In the first olivine<sub>1</sub> bearing field 30 wt % olivine with Mg# 68–92 is expected to produce a volume large enough to be detected in thin section. At the brucite-out boundary, however, Mg# 94–95 is in agreement with natural observations in olivine<sub>1</sub> and olivine<sub>2</sub> (Table 7). Overstepping of the olivine-in reaction by ~50 °C involving two hydrous phases seems unlikely. Moreover, Fe–Mg diffusive equilibration should not occur for this temperature range at the given time frame (Chakraborty 2010) and thus

cannot have obliterated a Fe-rich olivine. Antigorite and chlorite show Mg# 99 (Table 7) when modelled at brucite-out and the natural examples show Mg# 97 and Mg# 95 respectively. Brucite and antigorite show calculated Mg# 97 at olivine-in compared with Mg# 68 for olivine<sub>1</sub>. This discrepancy shows that calculated Mg# in antigorite, chlorite and possibly brucite are too high forcing iron to partition into olivine. This has the consequence that metamorphic olivine from the antigorite + brucite reaction starts forming at too low temperatures and shows an exaggerated fayalite component. Consequently, the divariant field where olivine and brucite coexist becomes too broad in the phase diagram. This effect is more accentuated when serpentinites with a reactive bulk of Mg# 90 is used instead of the local bulk map composition (Mg# = 96) where most bulk iron is stored in magnetite. For example, in the Zermatt-lherzolites, harzburgites and dunites, the divariant field between olivine-in and antigorite + brucite would expand from 376 to 501 °C ( $\Delta T = 125$  °C), 359–512 °C ( $\Delta T = 153$  °C) and 309–530 °C ( $\Delta T = 221$  °C) with olivine Mg# of 26–74, 21–80 and 11–89, respectively. Similar large ranges are observed for primitive mantle and IODP samples from meta-harzburgite and meta-dunite respectively (Table 7). On the contrary, even where magnetite has not extracted ferrous iron from the reactive phases such low Mg# in olivine are not attained in nature (Fig. 16). This suggests that the solution models for Mg–Fe exchange in brucite-antigorite-chlorite-olivine equilibria are insufficiently constrained and erroneously force ferrous iron partitioning into olivine relative to the other phases. Divariant fields must be significantly smaller (Trommsdorff and Evans 1972) since in natural examples Mg# < 85 are hardly attained around the world (Fig. 16) suggesting a width of the divariant field of ~20 °C (Fig. 12a). Even the lowest Mg# 80 olivines (Scambelluri et al. 1991) would extent the divariant field to only ~30 °C and little olivine could be produced between Mg# 80–85. This would reduce the extension of the divariant field, where olivine and brucite coexist, to less than 30 °C, and thus limit also the temperature interval, where fluid is released.

#### 4.6 Bulk rock fluid release from the antigorite + brucite reaction

The maximum and minimum weight percentage of fluid released from the antigorite + brucite reaction in the Zermatt-Saas serpentinites was forward modelled using *Perple\_X*'s subroutine *Meemum* in the *FMASH* and *CFMASH* system for dunites, harzburgites and lherzolites, respectively. The results of the modelling are summarized in Table 7. As discussed above, the amount of magnetite influences how much brucite is formed during serpentinization, which in

turn influences the amount of fluid that can be liberated at the antigorite + brucite reaction. All Fe is considered in the model as FeO resulting in a maximum estimate for the bulk fluid release. For the minimum estimate we imposed that all FeO was extracted from the system producing only olivine Mg# 100 at the termination of the reaction. A meta-dunite (MD) (Lg15), average meta-lherzolites (ML) and meta-harzburgite (MH) from Li et al. (2004b) and the local bulk map composition (this study) (Table 7) were used for the modelling. For  $\text{FeO} = \text{FeO}_{\text{tot}}$ , average MD, MH and ML water contents stored in solids prior to olivine growth is 15.1 wt%, 13.2 wt% and 11.7 wt%  $\text{H}_2\text{O}$ . The calculated bulk  $\text{H}_2\text{O}$  content in solids after olivine formation is 1.7 wt% (MD), 8.4 wt% (MH) and 8.3 wt% (ML)  $\text{H}_2\text{O}$ . This results in a highly variable amount of fluid that is produced during the antigorite + brucite reaction ranging from 13.4 wt% (MD) to 4.8 wt% (MH) to 3.4 wt%  $\text{H}_2\text{O}$  (ML). This amount is significantly reduced if  $\text{FeO}_{\text{tot}}$  is present as magnetite to 11.5 wt%, 0.8 wt% and 0.0 wt%  $\text{H}_2\text{O}$ , respectively. The local bulk composition from the map shows a modelled bulk  $\text{H}_2\text{O}$  content before and after olivine formation of 15.2 wt% and 2.8 wt%  $\text{H}_2\text{O}$  suggesting a maximum loss of 12.4 wt%  $\text{H}_2\text{O}$ . These calculations demonstrate that highly variable and especially for highly depleted serpentinites and dunites large quantities of  $\text{H}_2\text{O}$  can be liberated at the antigorite + brucite reaction.

The calculated  $\text{H}_2\text{O}$  values can be compared with the measured LOI's from Li et al. (2004b) assuming no carbonate contamination. The LOI are 3.6 wt% (MD), 11.3 wt% (MH) and 9.2 wt% (ML) consistently higher than the calculated  $\text{H}_2\text{O}$  contents of 1.7 wt% (MD), 8.4 wt% (MH) and 8.3 wt% (ML), respectively (Table 7). The reason for this is that late stage serpentinization has increased the LOIs. This illustrates that care has to be taken when measured LOI are used to constrain fluid loss during metamorphic reactions.

A summary of IODP bulk rock measurements of abyssal serpentinites is given in Deschamps et al. (2013). From the average bulk retrieved for harzburgite, a theoretical maximum of 13.8 wt%  $\text{H}_2\text{O}$  was present prior to olivine formation and 6.6 wt%  $\text{H}_2\text{O}$  was present after full antigorite + brucite consumption. This suggests a theoretical maximum average loss of 7.2 wt%  $\text{H}_2\text{O}$  during the antigorite + brucite reaction if no magnetite was present. The minimum release of 3.4 wt%  $\text{H}_2\text{O}$  in a fully serpentinized depleted harzburgite is calculated if all iron is present in magnetite. In the dunites the range lies between 4.9 and 9.4 wt%  $\text{H}_2\text{O}$  for Fe-free and  $\text{FeO}_{\text{tot}}$  bulks, respectively. For serpentinized primitive mantle if total iron is FeO then 2.9 wt%  $\text{H}_2\text{O}$  is released but if the bulk FeO is subtracted talc is formed instead of brucite.

#### 4.7 Implications of the antigorite + brucite reaction on thermodynamic and geodynamic models

In the literature, the antigorite + brucite reaction has been largely neglected in geodynamic models dealing with volatile recycling, partial melting, slab rheology, earth quakes and its significance in the deep water cycle e.g. (Deschamps et al. 2013; Hacker 2008; Peacock 2020; Rüpke et al. 2004; Schmidt and Poli 1998, 2014; Syracuse et al. 2010; van Keken et al. 2011). The reason for this might be grounded in the controversy about how abundantly brucite forms during serpentinization at mid-ocean ridges and in forearc settings and how much brucite there is in ultramafic rocks at the onset of subduction. For example, in the same IODP samples brucite was identified in one study whereas the other did not (Bach et al. 2004; Vils et al. 2008) showing the difficulty to spot this phase. Additionally, a clear set of criteria to identify olivine that formed through the antigorite + brucite reaction were missing.

Published phase diagrams and thermal models of subduction zones considering the serpentinite reactions commonly use bulk serpentinite or peridotite analyses of various compositions (Hacker 2008; Hacker et al. 2003; Schmidt and Poli 1998; van Keken et al. 2011) for modelling the P–T estimates and fluid release. There are several pitfalls that can occur in such calculations: (1) The antigorite + brucite reaction is ignored leading to an overestimation of the amount of water released at the antigorite breakdown. (2) The Tschermak component in antigorite is not considered, resulting in dehydration reactions involving antigorite that are too low in temperature by 30–50 °C (Padrón-Navarta et al. 2013). (3) The divariant field in which olivine and brucite coexist is too large, resulting in a much larger temperature interval for fluid release at the antigorite + brucite reaction (see discussion above). (4) The effect of magnetite on phase relations and fluid release is not taken into consideration. (5) Commonly, a single peridotite composition is chosen and thus the considerable effect of variable bulk composition on the position of the antigorite + brucite reaction as well as on the amount of fluid released is not taken into account.

## 5 Conclusions

A single serpentinite outcrop at the lower Theodulglier in the Zermatt-Saas unit documents a full orogenic cycle from mantle exhumation, to seafloor alteration, subduction and exhumation. The dehydration reaction of antigorite + brucite to olivine + chlorite +  $\text{H}_2\text{O}$  is exceptionally well preserved in this outcrop. In undeformed serpentinites, the occurrence of metamorphic olivine can be used to map out the previous distribution of brucite in seafloor-altered mantle rocks. In deformed serpentinites, metamorphic olivine marks

the pathways of the escaping fluid in a network of veins and shear zones. Metamorphic olivine is characterized by highly variable Mg#, low Ni, Ca, Ti, Al and high B and Mn contents. Up to 140  $\mu\text{g/g}$  of  $\text{H}_2\text{O}$  is found exclusively in Si vacancies. The majority of olivine formation and fluid release, occurred within a narrow field  $< 30^\circ\text{C}$  between 550 and 600  $^\circ\text{C}$  at fore-arc depths of 60–80 km, liberating between 3.4 and 7.2 wt%  $\text{H}_2\text{O}$  for a depleted, fully serpentinized harzburgitic composition. The large amount of focused fluid released over a small temperature interval might trigger eclogite formation in the overlying meta-basalts, meta-gabbros, metarodingites and metasediments and could be responsible for earthquakes registered in the oceanic lithosphere at fore-arc depths.

## Supplementary information

**Supplementary information** accompanies this paper at <https://doi.org/10.1186/s00015-020-00368-0>.

**Additional file 1: Table S1.** List of samples used in this study corresponding with locations in Fig. 2.

**Additional file 2: Figure S2.** **a** Sample FA, large olivine<sub>1</sub> with sulphide inclusions. **b** Sample FA, olivine<sub>2</sub> domain no sulphides present. **c** Sample OL<sub>2</sub>, olivine<sub>2</sub>-rich and sulphide absent domain. **d** Sample OL<sub>2</sub>, partially retrogressed sulphide-rich domain.

**Additional file 3: Table S2.** Full data set of EPMA analyses for all phases.

**Additional file 4: Figure S3.** Left: Sample 14, Ti-chondrodite grain with Atg, Chl, Di, Ol, Mt. Right: Ilmenite grain in sample 14.

**Additional file 5: Figure S4.** Sample FA, the white rectangle indicates the area mapped in Fig. 10. Lower part: Large olivine<sub>1</sub> single crystal includes magnetite mesh polygons. Upper part: Small polygonal olivine<sub>2</sub> generation in textural equilibrium with chlorite and Ti-clinohumite.

**Additional file 6: Table S4.** FTIR analyses of the Ti-clinohumite lamellae bearing olivine<sub>1</sub> generation.

**Additional file 7: Table S3.** Full data set of EPMA analyses used in Figs. 9 and 14 of spinel group minerals from Piccardo and Vissers (2007), Vils et al. (2008), Pirard et al. (2013) and Müntener (1997).

**Additional file 8: Figure S1.** Drone image from the area indicated by the black rectangle in Fig. 2. Sample localities are indicated with rectangles.

## Acknowledgements

We thank D. Marty and P. Manzotti for editorial handling and M. Scambelluri and an anonymous reviewer for helpful comments on this paper. H. and L. Kempf are gratefully acknowledged for the physically tough work and technical support during the extensive sampling campaign. T. Good is thanked for taking the drone images and J.A.D. Connolly for discussions about phase diagrams. We thank T. Pettke for the help with LA-ICP-MS measurements. J. Reynes and P. Tollan are thanked for discussions about FTIR. We also thank Othmar Müntener for providing spinel compositional data. This work was financially supported by the Swiss National Science Foundation project 200021\_169062.

## Authors' contributions

This work resulted from the Masters and PhD thesis of EDK. EDK conducted the fieldwork, all analytical work and thermodynamic modelling. ER and LPB supervised the Masters and JH the PhD projects. PL assisted in the quantitative mapping and data processing. EDK and JH wrote the paper with input from all authors. JH secured the funding. All authors read and approved the final manuscript.

## Availability of data

All samples, including thin and thick sections are stored at the Institute of Geological Sciences at the University of Bern, Bern, Switzerland. All data analysed during this study are included in the article and additional Tables S1–S4 and Figures S1–S4.

## Competing interests

The authors declare that there are no competing interests.

## Author details

<sup>1</sup> Institute of Geological Sciences, University of Bern, Baltzerstrasse 1+3, 3012 Bern, Switzerland. <sup>2</sup> Institute of Geochemistry and Petrology, ETH Zurich, Clausiusstrasse 25, 8092 Zurich, Switzerland. <sup>3</sup> Institute of Earth Sciences, University of Lausanne, Quartier UNIL-Mouline Batiment Géopolis 4885, 1015 Lausanne, Switzerland.

Received: 15 April 2020 Accepted: 25 August 2020

Published online: 26 October 2020

## References

- Agard, P., Yamato, P., Jolivet, L., & Burov, E. (2009). Exhumation of oceanic blueschists and eclogites in subduction zones: timing and mechanisms. *Earth-Science Reviews*, 92(1), 53–79. <https://doi.org/10.1016/j.earscirev.2008.11.002>.
- Angiboust, S., Agard, P., Jolivet, L., & Beyssac, O. (2009). The Zermatt-Saas ophiolite: the largest (60-km wide) and deepest (c. 70–80 km) continuous slice of oceanic lithosphere detached from a subduction zone? *Terra Nova*, 21(3), 171–180. <https://doi.org/10.1111/j.1365-3121.2009.00870.x>.
- Arai, S., Ishimaru, S., & Mizukami, T. (2012). Methane and propane micro-inclusions in olivine in titanoclinohumite-bearing dunites from the Sanbagawa high-P metamorphic belt, Japan: Hydrocarbon activity in a subduction zone and Ti mobility. *Earth and Planetary Science Letters*, 353, 1–11. <https://doi.org/10.1016/j.epsl.2012.07.043>.
- Bach, W., Garrido, C. J., Paulick, H., Harvey, J., & Rosner, M. (2004). Seawater-peridotite interactions: First insights from ODP Leg 209, MAR 15 N. *Geochemistry, Geophysics, Geosystems*. <https://doi.org/10.1029/2004gc000744>.
- Bach, W., Paulick, H., Garrido, C. J., Ildefonse, B., Meurer, W. P., & Humphris, S. E. (2006). Unraveling the sequence of serpentinization reactions: petrography, mineral chemistry, and petrophysics of serpentinites from MAR 15 N (ODP Leg 209, Site 1274). *Geophysical Research Letters*. <https://doi.org/10.1029/2006gl025681>.
- Beard, J. S., & Frost, R. B. (2016). The stoichiometric effects of ferric iron substitutions in serpentine from microprobe data. *International Geology Review*, 59(5–6), 541–547. <https://doi.org/10.1080/00206814.2016.1197803>.
- Beard, J. S., Frost, R. B., Fryer, P., McCaig, A., Searle, R., Ildefonse, B., et al. (2009). Onset and progression of serpentinization and magnetite formation in olivine-rich troctolite from IODP Hole U1309D. *Journal of Petrology*, 50(3), 387–403. <https://doi.org/10.1093/petrology/egp004>.
- Bearth, P. (1967). Die Ophiolithe der Zone von Zermatt-Saas Fee. *Beiträge zur geologischen Karte der Schweiz, N.F.* 132, 130.
- Bell, D. R., Rossman, G. R., Maldener, J., Endisch, D., & Rauch, F. (2003). Hydroxide in olivine: A quantitative determination of the absolute amount and calibration of the IR spectrum. *Journal of Geophysical Research: Solid Earth*, 108(B2), 2015–2113. <https://doi.org/10.1029/2001JB000679>.
- Bill, M., Bussy, F. O., Cosca, M., Masson, H., & Hunziker, J. C. (1997). High-precision U-Pb and 40Ar/39Ar dating of an Alpine ophiolite (Gets nappe, French Alps). *Eclogae Geologicae Helvetiae*, 90, 43–54. <https://doi.org/10.5169/seals-168144>.
- Bloch, W., John, T., Kummerow, J., Salazar, P., Krüger, O. S., & Shapiro, S. A. (2018). Watching dehydration: Seismic indication for transient fluid pathways in the oceanic mantle of the subducting Nazca Slab. *Geochemistry, Geophysics, Geosystems*, 19(9), 3189–3207. <https://doi.org/10.1029/2018GC007703>.
- Bowen, N. L., & Tuttle, O. F. (1949). The system  $\text{MgO}-\text{SiO}_2-\text{H}_2\text{O}$ . *Geological Society of America Bulletin*, 60(3), 439–460. [https://doi.org/10.1130/0016-7606\(1949\)60%5b439:tsm%5d2.0.co;2](https://doi.org/10.1130/0016-7606(1949)60%5b439:tsm%5d2.0.co;2).
- Bromiley, G. D., & Pawley, A. R. (2003). The stability of antigorite in the systems  $\text{MgO}-\text{SiO}_2-\text{H}_2\text{O}$  (MSH) and  $\text{MgO}-\text{Al}_2\text{O}_3-\text{SiO}_2-\text{H}_2\text{O}$  (MASH): The effects of

- Al<sup>3+</sup> substitution on high-pressure stability. *American Mineralogist*, 88(1), 99–108. <https://doi.org/10.2138/am-2003-0113>.
- Bucher, K., Fazis, Y., De Capitani, C., & Grapes, R. (2005). Blueschists, eclogites, and decompression assemblages of the Zermatt-Saas ophiolite: High-pressure metamorphism of subducted Tethys lithosphere. *American Mineralogist*, 90(5–6), 821–835. <https://doi.org/10.2138/am.2005.1718>.
- Bucher, K., & Grapes, R. (2009). The eclogite-facies Allalin Gabbro of the Zermatt-Saas ophiolite, Western Alps: a record of subduction zone hydration. *Journal of Petrology*, 50(8), 1405–1442. <https://doi.org/10.1093/ptrology/egp035>.
- Cartwright, I., & Barnicoat, A. C. (1999). Stable isotope geochemistry of Alpine ophiolites: a window to ocean-floor hydrothermal alteration and constraints on fluid–rock interaction during high-pressure metamorphism. *International Journal of Earth Sciences*, 88(2), 219–235. <https://doi.org/10.1007/s005310050261>.
- Cartwright, I., & Barnicoat, A. (2002). Petrology, geochronology, and tectonics of shear zones in the Zermatt-Saas and Combin zones of the Western Alps. *Journal of Metamorphic Geology*, 20(2), 263–281. <https://doi.org/10.1046/j.0263-4929.2001.00366.x>.
- Chakraborty, S. (2010). Diffusion coefficients in olivine, wadsleyite and ringwoodite. *Reviews in Mineralogy and Geochemistry*, 72(1), 603–639. <https://doi.org/10.2138/rmg.2010.72.13>.
- Coleman, R., & Keith, T. (1971). A chemical study of serpentinization—Burro Mountain, California. *Journal of Petrology*, 12(2), 311–328. <https://doi.org/10.1093/ptrology/12.2.311>.
- Connolly, J. (2009). The geodynamic equation of state: what and how. *Geochimistry, Geophysics, Geosystems*. <https://doi.org/10.1029/2009gc002540>.
- De Hoog, J. C., Gall, L., & Cornell, D. H. (2010). Trace-element geochemistry of mantle olivine and application to mantle petrogenesis and geothermobarometry. *Chemical Geology*, 270(1–4), 196–215. <https://doi.org/10.1016/j.chemgeo.2009.11.017>.
- de Meyer, C. M., Baumgartner, L. P., Beard, B. L., & Johnson, C. M. (2014). Rb–Sr ages from phengite inclusions in garnets from high pressure rocks of the Swiss Western Alps. *Earth and Planetary Science Letters*, 395, 205–216. <https://doi.org/10.1016/j.epsl.2014.03.050>.
- Deschamps, F., Godard, M., Guillot, S., & Hattori, K. (2013). Geochemistry of subduction zone serpentinites: A review. *Lithos*, 178, 96–127. <https://doi.org/10.1016/j.lithos.2013.05.019>.
- Dobson, D. P., Meredith, P. G., & Boon, S. A. (2002). Simulation of subduction zone seismicity by dehydration of serpentine. *Science*, 298(5597), 1407–1410. <https://doi.org/10.1126/science.1075390>.
- Escher, A., & Beaumont, C. (1997). Formation, burial and exhumation of basement nappes at crustal scale: a geometric model based on the Western Swiss-Italian Alps. *Journal of Structural Geology*, 19(7), 955–974. [https://doi.org/10.1016/S0191-8141\(97\)00022-9](https://doi.org/10.1016/S0191-8141(97)00022-9).
- Evans, B. W. (2004). The serpentinite multisystem revisited: chrysotile is metastable. *International Geology Review*, 46(6), 479–506. <https://doi.org/10.2747/0020-6814.46.6.479>.
- Evans, B. W., & Trommsdorff, V. (1978). Petrogenesis of garnet lherzolite, Cima di Gagnone, Lepontine Alps. *Earth and Planetary Science Letters*, 40(3), 333–348. [https://doi.org/10.1016/0012-821X\(78\)90158-9](https://doi.org/10.1016/0012-821X(78)90158-9).
- Faul, U. H., Cline, C. J., David, E. C., Berry, A. J., & Jackson, I. (2016). Titanium-hydroxyl defect-controlled rheology of the Earth's upper mantle. *Earth and Planetary Science Letters*, 452, 227–237. <https://doi.org/10.1016/j.epsl.2016.07.016>.
- Ferrand, T. P., Hilairet, N., Incel, S., Deldicque, D., Labrousse, L., Gasc, J., et al. (2017). Dehydration-driven stress transfer triggers intermediate-depth earthquakes. *Nature communications*, 8(1), 1–11. <https://doi.org/10.1038/ncomms15247>.
- Frost, R. B. (1985). On the stability of sulfides, oxides, and native metals in serpentinite. *Journal of Petrology*, 26(1), 31–63. <https://doi.org/10.1093/ptrology/26.1.31>.
- Frost, R. B., & Beard, J. S. (2007). On silica activity and serpentinization. *Journal of Petrology*, 48(7), 1351–1368. <https://doi.org/10.1093/ptrology/egm021>.
- Früh-Green, G. L., Connolly, J. A., Plas, A., Kelley, D. S., & Grobéty, B. (2004). Serpentinization of oceanic peridotites: Implications for geochemical cycles and biological activity. *GMS*, 144, 119–136. <https://doi.org/10.1029/144GM08>.
- Garrido, C. J., López Sánchez-Vizcaino, V., Gómez-Pugnaire, M. T., Trommsdorff, V., Alard, O., Bodinier, J. L., et al. (2005). Enrichment of HFSE in chlorite-harzburgite produced by high-pressure dehydration of antigorite-serpentinite: Implications for subduction magmatism. *Geochimistry, Geophysics, Geosystems*. <https://doi.org/10.1029/2004gc000791>.
- Gasc, J., Hilairet, N., Yu, T., Ferrand, T., Schubnel, A., & Wang, Y. (2017). Faulting of natural serpentinite: Implications for intermediate-depth seismicity. *Earth and Planetary Science Letters*, 474, 138–147. <https://doi.org/10.1016/j.epsl.2017.06.016>.
- Gerya, T. V., Stöckhert, B., & Perchuk, A. L. (2002). Exhumation of high-pressure metamorphic rocks in a subduction channel: A numerical simulation. *Tectonics*, 21(6), 6–1–6–19. <https://doi.org/10.1029/2002tc001406>.
- Gilio, M., Scambelluri, M., Agostini, S., Godard, M., Peters, D., & Pettke, T. (2019). Petrology and geochemistry of serpentinites associated with the ultra-high pressure Lago di Cignana Unit (Italian Western Alps). *Journal of Petrology*, 60(6), 1229–1262. <https://doi.org/10.1093/ptrology/egz030>.
- Guillong, M., Meier, D. L., Allan, M. M., Heinrich, C. A., & Yardley, B. W. (2008). Appendix A6: SILL: A MATLAB-based program for the reduction of laser ablation ICP-MS data of homogeneous materials and inclusions. *Mineralogical Association of Canada Short Course*, 40, 328–333.
- Guillot, S., Schwartz, S., Reynard, B., Agard, P., & Prigent, C. (2015). Tectonic significance of serpentinites. *Tectonophysics*, 646, 1–19. <https://doi.org/10.1016/j.tecto.2015.01.020>.
- Hacker, B. R. (2008). H<sub>2</sub>O subduction beyond arcs. *Geochimistry, Geophysics, Geosystems*. <https://doi.org/10.1029/2007gc001707>.
- Hacker, B. R., Peacock, S. M., Abers, G. A., & Hollaway, S. D. (2003). Subduction factory 2. Are intermediate-depth earthquakes in subducting slabs linked to metamorphic dehydration reactions? *Journal of Geophysical Research*. <https://doi.org/10.1029/2001jb001129>.
- Harvey, J., Garrido, C. J., Savov, I., Agostini, S., Padrón-Navarta, J. A., Marchesi, C., et al. (2014). 11B-rich fluids in subduction zones: The role of antigorite dehydration in subducting slabs and boron isotope heterogeneity in the mantle. *Chemical Geology*, 376, 20–30. <https://doi.org/10.1016/j.chemgeo.2014.03.015>.
- Hellebrand, E., Snow, J. E., Dick, H. J., & Hofmann, A. W. (2001). Coupled major and trace elements as indicators of the extent of melting in mid-ocean-ridge peridotites. *Nature*, 410(6829), 677. <https://doi.org/10.1038/35070546>.
- Hellebrand, E., Snow, J. E., & Mühe, R. (2002). Mantle melting beneath Gakkel Ridge (Arctic Ocean): abyssal peridotite spinel compositions. *Chemical Geology*, 182(2–4), 227–235. [https://doi.org/10.1016/S0009-2541\(01\)00291-1](https://doi.org/10.1016/S0009-2541(01)00291-1).
- Hermann, J., O'Neill, H. S. C., & Berry, A. (2005). Titanium solubility in olivine in the system TiO<sub>2</sub>–MgO–SiO<sub>2</sub>: no evidence for an ultra-deep origin of Ti-bearing olivine. *Contributions to Mineralogy and Petrology*, 148(6), 746–760. <https://doi.org/10.1007/s00410-004-0637-4>.
- Hirschmann, M. M., Ghiorso, M. S., Waslylenki, L., Asimow, P. D., & Stolper, E. M. (1998). Calculation of peridotite partial melting from thermodynamic models of minerals and melts. I. Review of methods and comparison with experiments. *Journal of Petrology*, 39(6), 1091–1115. <https://doi.org/10.1093/ptrology/39.6.1091>.
- Holland, T., Baker, J., & Powell, R. (1998). Mixing properties and activity-composition relationships of chlorites in the system MgO–FeO–Al<sub>2</sub>O<sub>3</sub>–SiO<sub>2</sub>–H<sub>2</sub>O. *European Journal of Mineralogy*. <https://doi.org/10.1127/ejm/10/3/0395>.
- Holland, T., & Powell, R. (1998). An internally consistent thermodynamic data set for phases of petrological interest. *Journal of Metamorphic Geology*, 16(3), 309–343. <https://doi.org/10.1111/j.1525-1314.1998.00140.x>.
- Hostetler, P., Coleman, R., Mumpton, F., & Evans, B. (1966). Brucite in alpine serpentinites. *American Mineralogist: Journal of Earth and Planetary Materials*, 51(1–2), 75–98.
- Jollands, M. C., Kempf, E. D., Hermann, J., & Müntener, O. (2019). Coupled inter-site reaction and diffusion: Rapid dehydrogenation of silicon vacancies in natural olivine. *Geochimica et Cosmochimica Acta*, 262, 220–242. <https://doi.org/10.1016/j.gca.2019.07.025>.
- Jung, H., & Green, H. W. (2004). Experimental faulting of serpentinite during dehydration: Implications for earthquakes, seismic low-velocity zones, and anomalous hypocenter distributions in subduction zones. *International Geology Review*, 46(12), 1089–1102. <https://doi.org/10.2747/0020-6814.46.12.1089>.
- Kawahara, H., Endo, S., Wallis, S. R., Nagaya, T., Mori, H., & Asahara, Y. (2016). Brucite as an important phase of the shallow mantle wedge: Evidence from the Shiraga unit of the Sanbagawa subduction zone, SW Japan. *Lithos*, 254, 53–66. <https://doi.org/10.1016/j.lithos.2016.02.022>.

- Kempf, E. D., & Hermann, J. (2018). Hydrogen incorporation and retention in metamorphic olivine during subduction: Implications for the deep water cycle. *Geology*, 46(6), 571–574. <https://doi.org/10.1130/G40120.1>.
- Kent, A. J., & Rossman, G. R. (2002). Hydrogen, lithium and boron in mantle-derived olivine: The role of coupled substitutions. *American Mineralogist*, 87, 1432–1436. <https://doi.org/10.2138/am-2002-1020>.
- Klein, F., Bach, W., Humphris, S. E., Kahl, W.-A., Jöns, N., Moskowit, B., et al. (2014). Magnetite in seafloor serpentinite—Some like it hot. *Geology*, 42(2), 135–138. <https://doi.org/10.1130/G35068.1>.
- Kodolányi, J., Pettke, T., Spandler, C., Kamber, B. S., & Gméling, K. (2011). Geochemistry of ocean floor and fore-arc serpentinites: constraints on the ultramafic input to subduction zones. *Journal of Petrology*, 53(2), 235–270. <https://doi.org/10.1093/ptrology/egr058>.
- Kunugiza, K. (1982). Formation of zoning of olivine with progressive metamorphism of serpentinite—an example from the Ryumon peridotite body of the Sanbagawa metamorphic belt, Kii peninsula. *The Journal of the Japanese Association of Mineralogists, Petrologists and Economic Geologists*, 77(5), 157–170. <https://doi.org/10.2465/ganko1941.77.157>.
- Lanari, P., & Engi, M. (2017). Local bulk composition effects on metamorphic mineral assemblages. *Rev Mineral Geochem*, 83(1), 55–102. <https://doi.org/10.2138/rmg.2017.83.3>.
- Lanari, P., Vho, A., Bovay, T., Airaghi, L., & Centrella, S. (2019). Quantitative compositional mapping of mineral phases by electron probe micro-analyser. *Geological Society, London, Special Publications*, 478(1), 39–63. <https://doi.org/10.1144/SP478.4>.
- Lanari, P., Vidal, O., De Andrade, V., Dubacq, B., Lewin, E., Grosch, E. G., et al. (2014). XMapTools: A MATLAB®-based program for electron microprobe X-ray image processing and geothermobarometry. *Computers & Geosciences*, 62, 227–240. <https://doi.org/10.1016/j.cageo.2013.08.010>.
- Lapen, T. J., Johnson, C. M., Baumgartner, L. P., Mahlen, N. J., Beard, B. L., & Amato, J. M. (2003). Burial rates during prograde metamorphism of an ultra-high-pressure terrane: an example from Lago di Cignana, western Alps, Italy. *Earth and Planetary Science Letters*, 215(1–2), 57–72. [https://doi.org/10.1016/S0012-821X\(03\)00455-2](https://doi.org/10.1016/S0012-821X(03)00455-2).
- Li, X. P., Rahn, M., & Bucher, K. (2004a). Metamorphic processes in rodingites of the Zermatt-Saas ophiolites. *International Geology Review*, 46(1), 28–51. <https://doi.org/10.2747/0020-6814.46.1.28>.
- Li, X. P., Rahn, M., & Bucher, K. (2004b). Serpentinites of the Zermatt-Saas ophiolite complex and their texture evolution. *Journal of Metamorphic Geology*, 22(3), 159–177. <https://doi.org/10.1111/j.1525-1314.2004.00503.x>.
- Li, X. P., Rahn, M., & Bucher, K. (2008). Eclogite facies metarodingites-phase relations in the system SiO<sub>2</sub>-Al<sub>2</sub>O<sub>3</sub>-Fe<sub>2</sub>O<sub>3</sub>-FeO-MgO-CaO-CO<sub>2</sub>-H<sub>2</sub>O: an example from the Zermatt-Saas ophiolite. *Journal of Metamorphic Geology*, 26(3), 347–364. <https://doi.org/10.1111/j.1525-1314.2008.00761.x>.
- Luoni, P., Rebay, G., Spalla, M. I., & Zanon, D. (2018). UHP Ti-chondroite in the Zermatt-Saas serpentinite: Constraints on a new tectonic scenario. *American Mineralogist: Journal of Earth and Planetary Materials*, 103(6), 1002–1005. <https://doi.org/10.2138/am-2018-6460>.
- Marchesi, C., Garrido, C. J., Harvey, J., González-Jiménez, J. M., Hidas, K., Lorand, J.-P., et al. (2013). Platinum-group elements, S, Se and Cu in highly depleted abyssal peridotites from the Mid-Atlantic Ocean Ridge (ODP Hole 1274A): influence of hydrothermal and magmatic processes. *Contributions to Mineralogy and Petrology*, 166(5), 1521–1538. <https://doi.org/10.1007/s00410-013-0942-x>.
- McDonough, W. F., & Rudnick, R. L. (1999). Mineralogy and composition of the upper mantle. *Reviews in Mineralogy*, 37, 139–164. <https://doi.org/10.2138/rmg.1999.37.4>.
- McDonough, W. F., & Sun, S.-S. (1995). The composition of the Earth. *Chemical Geology*, 120, 223–253. [https://doi.org/10.1016/0009-2541\(94\)00140-4](https://doi.org/10.1016/0009-2541(94)00140-4).
- Mellini, M., Trommsdorff, V., & Compagnoni, R. (1987). Antigorite polydeformation: behaviour during progressive metamorphism. *Contributions to Mineralogy and Petrology*, 97(2), 147–155. <https://doi.org/10.1007/BF00371235>.
- Merkulova, M., Muñoz, M., Brunet, F., Vidal, O., Hattori, K., Vantelon, D., et al. (2017). Experimental insight into redox transfer by iron- and sulfur-bearing serpentinite dehydration in subduction zones. *Earth and Planetary Science Letters*, 479, 133–143. <https://doi.org/10.1016/j.epsl.2017.09.009>.
- Moody, J. B. (1976). Serpentinization: a review. *Lithos*, 9(2), 125–138. [https://doi.org/10.1016/0024-4937\(76\)90030-X](https://doi.org/10.1016/0024-4937(76)90030-X).
- Müntener, O. (1997). *The Malenco peridotites (Alps): petrology and geochemistry of subcontinental mantle and Jurassic exhumation during rifting*. (Ph.D. Thesis), ETH Zurich.
- Müntener, O., & Hermann, J. (1996). The Val Malenco lower crust–upper mantle complex and its field relations (Italian Alps). *Schweizerische Mineralogische und Petrographische Mitteilungen*, 76(3), 475–500. <https://doi.org/10.5169/seals-57711>.
- Müntener, O., & Hermann, J. (2001). The role of lower crust and continental upper mantle during formation of non-volcanic passive margins: evidence from the Alps. *Geological Society, London, Special Publications*, 187(1), 267–288. <https://doi.org/10.1144/GSL.SP.2001.187.01.13>.
- Nozaka, T. (2003). Compositional heterogeneity of olivine in thermally metamorphosed serpentinite from Southwest Japan. *American Mineralogist*, 88(8–9), 1377–1384. <https://doi.org/10.2138/am-2003-8-922>.
- O’Hanley, D. S. (1996). *Serpentinites: records of tectonic and petrological history*. Oxford University Press on Demand.
- O’Hanley, D. S., & Dyar, M. D. (1993). The composition of lizardite 1T and the formation of magnetite in serpentinites. *American Mineralogist*, 78(3–4), 391–404.
- Padrón-Navarta, J., & Hermann, J. (2017). A subsolidus olivine water solubility equation for the Earth’s upper mantle. *Journal of Geophysical Research: Solid Earth*. <https://doi.org/10.1002/2017jb014510>.
- Padrón-Navarta, J. A., Hermann, J., Garrido, C. J., Sánchez-Vizcaino, V. L., & Gómez-Pugnaire, M. T. (2010). An experimental investigation of antigorite dehydration in natural silica-enriched serpentinite. *Contributions to Mineralogy and Petrology*, 159(1), 25–42. <https://doi.org/10.1007/s00410-009-0414-5>.
- Padrón-Navarta, J. A., Lopez Sanchez-Vizcaino, V., Garrido, C. J., & Gómez-Pugnaire, M. T. (2011). Metamorphic record of high-pressure dehydration of antigorite serpentinite to chlorite harzburgite in a subduction setting (Cerro del Almirez, Nevado-Filábride Complex, Southern Spain). *Journal of Petrology*, 52(10), 2047–2078. <https://doi.org/10.1093/ptrology/egr039>.
- Padrón-Navarta, J. A., Sánchez-Vizcaino, V. L., Hermann, J., Connolly, J. A., Garrido, C. J., Gómez-Pugnaire, M. T., et al. (2013). Tschermak’s substitution in antigorite and consequences for phase relations and water liberation in high-grade serpentinites. *Lithos*, 178, 186–196. <https://doi.org/10.1016/j.lithos.2013.02.001>.
- Peacock, S. M. (2001). Are the lower planes of double seismic zones caused by serpentine dehydration in subducting oceanic mantle? *Geology*, 29(4), 299–302. [https://doi.org/10.1130/0091-7613\(2001\)029%3C0299:ATLPOD%3E2.0.CO;2](https://doi.org/10.1130/0091-7613(2001)029%3C0299:ATLPOD%3E2.0.CO;2).
- Peacock, S. M. (2020). Advances in the thermal and petrologic modeling of subduction zones. *Geosphere*. <https://doi.org/10.1130/GES02213.1>.
- Peretti, A., Dubessy, J., Mullis, J., Frost, B. R., & Trommsdorff, V. (1992). Highly reducing conditions during Alpine metamorphism of the Malenco peridotite (Sondrio, northern Italy) indicated by mineral paragenesis and H<sub>2</sub> in fluid inclusions. *Contributions to Mineralogy and Petrology*, 112(2–3), 329–340. <https://doi.org/10.1007/BF00310464>.
- Peters, D., Pettke, T., John, T., & Scambelluri, M. (2020). The role of brucite in water and element cycling during serpentinite subduction—Insights from Erro Tobbio (Liguria, Italy). *Lithos*, 360–361, 1–15. <https://doi.org/10.1016/j.lithos.2020.105431>.
- Pettke, T., Oberli, F., Audétat, A., Guillong, M., Simon, A. C., Hanley, J. J., et al. (2012). Recent developments in element concentration and isotope ratio analysis of individual fluid inclusions by laser ablation single and multiple collector ICP-MS. *Ore Geology Reviews*, 44, 10–38. <https://doi.org/10.1016/j.oregeorev.2011.11.001>.
- Piccardo, G. B., Rampone, E., & Vannucci, R. (1990). Upper mantle evolution during continental rifting and ocean formation: evidences from peridotite bodies of the western Alpine-northern Apennine system. *Mémoires de la Société géologique de France*, 156, 323–333.
- Piccardo, G., & Vissers, R. (2007). The pre-oceanic evolution of the Erro-Tobbio peridotite (Voltri Massif, Ligurian Alps, Italy). *Journal of Geodynamics*, 43(4–5), 417–449. <https://doi.org/10.1016/j.jog.2006.11.001>.
- Piccoli, F., Hermann, J., Pettke, T., Connolly, J. A. D., Kempf, E. D., & Vieira Duarte, J. F. (2019). Subducting serpentinites release reduced, not oxidized, aqueous fluids. *Scientific Reports*, 9(1), 19573. <https://doi.org/10.1038/s41598-019-55944-8>.
- Pirard, C., Hermann, J., & O’Neill, H. S. C. (2013). Petrology and geochemistry of the crust–mantle boundary in a nascent arc, Massif du Sud ophiolite, New Caledonia, SW Pacific. *Journal of Petrology*, 54(9), 1759–1792. <https://doi.org/10.1093/ptrology/egt030>.

- Plümper, O., Botan, A., Los, C., Liu, Y., Malthé-Sørenssen, A., & Jamtveit, B. (2017a). Fluid-driven metamorphism of the continental crust governed by nanoscale fluid flow. *Nature Geoscience*, *10*(9), 685. <https://doi.org/10.1038/ngeo3009>.
- Plümper, O., John, T., Podladchikov, Y. Y., Vrijmoed, J. C., & Scambelluri, M. (2017b). Fluid escape from subduction zones controlled by channel-forming reactive porosity. *Nature Geoscience*, *10*(2), 150. <https://doi.org/10.1038/ngeo2865>.
- Rahn, M., & Rahn, K. (1998). Titanian clinohumite formation in the Zermatt-Saas ophiolites, central Alps. *Mineralogy and Petrology*, *64*(1–4), 1–13. <https://doi.org/10.1007/BF01226561>.
- Rampone, E., Romairone, A., Abouchami, W., Piccardo, G., & Hofmann, A. (2005). Chronology, petrology and isotope geochemistry of the Erro-Tobbio peridotites (Ligurian Alps, Italy): records of Late Palaeozoic lithospheric extension. *Journal of Petrology*, *46*(4), 799–827. <https://doi.org/10.1093/ptrology/egi001>.
- Reinecke, T. (1991). Very-high-pressure metamorphism and uplift of coesite-bearing metasediments from the Zermatt-Saas zone. *Western Alps. European Journal of Mineralogy*. <https://doi.org/10.1127/ejm/3/1/0007>.
- Rubatto, D., Gebauer, D., & Fanning, M. (1998). Jurassic formation and Eocene subduction of the Zermatt–Saas-Fee ophiolites: implications for the geodynamic evolution of the Central and Western Alps. *Contributions to Mineralogy and Petrology*, *132*(3), 269–287. <https://doi.org/10.1007/s004100050421>.
- Rüpke, L. H., Morgan, J. P., Hort, M., & Connolly, J. A. (2004). Serpentine and the subduction zone water cycle. *Earth and Planetary Science Letters*, *223*(1–2), 17–34. <https://doi.org/10.1016/j.epsl.2004.04.018>.
- Ryan, J. G., & Chauvel, C. (2014). The subduction-zone filter and the impact of recycled materials on the evolution of the mantle. *Treatise on Geochemistry 2nd Edition*, *3*, 479–508. <https://doi.org/10.1016/B978-0-08-095975-7-00211-4>.
- Savov, I. P., Ryan, J. G., D'Antonio, M., Kelley, K., & Mattie, P. (2005). Geochemistry of serpentized peridotites from the Mariana Forearc Conical Seamount, ODP Leg 125: Implications for the elemental recycling at subduction zones. *Geochemistry, Geophysics, Geosystems*. <https://doi.org/10.1029/2004gc000777>.
- Scambelluri, M., Cannao, E., & Gilio, M. (2019). The water and fluid-mobile element cycles during serpentinite subduction. A review. *European Journal of Mineralogy*, *31*(3), 405–428. <https://doi.org/10.1127/ejm/2019/0031-2842>.
- Scambelluri, M., Müntener, O., Hermann, J. R., Piccardo, G. B., & Trommsdorff, V. (1995). Subduction of water into the mantle: history of an Alpine peridotite. *Geology*, *23*(5), 459–462. [https://doi.org/10.1130/0091-7613\(1995\)023%3c0459:SOWITM%3e2.3.CO;2](https://doi.org/10.1130/0091-7613(1995)023%3c0459:SOWITM%3e2.3.CO;2).
- Scambelluri, M., Müntener, O., Ottolini, L., Pettker, T., & Vannucci, R. (2004). The fate of B, Cl and Li in the subducted oceanic mantle and in the antigorite-breakdown fluids. *Earth and Planetary Science Letters*, *222*, 217–234. <https://doi.org/10.1016/j.epsl.2004.02.012>.
- Scambelluri, M., Pettker, T., Rampone, E., Godard, M., & Reusser, E. (2014). Petrology and trace element budgets of high-pressure peridotites indicate subduction dehydration of serpentinitized mantle (Cima di Gagnone, Central Alps, Switzerland). *Journal of Petrology*, *55*(3), 459–498. <https://doi.org/10.1093/ptrology/egt068>.
- Scambelluri, M., & Rampone, E. (1999). Mg-metasomatism of oceanic gabbros and its control on Ti-clinohumite formation during eclogitization. *Contributions to Mineralogy and Petrology*, *135*(1), 1–17. <https://doi.org/10.1007/s004100050494>.
- Scambelluri, M., Rampone, E., & Piccardo, G. (2001). Fluid and element cycling in subducted serpentinite: A trace-element study of the Erro-Tobbio high-pressure ultramafites (Western Alps, NW Italy). *Journal of Petrology*, *42*, 55–67. <https://doi.org/10.1093/ptrology/42.1.55>.
- Scambelluri, M., Strating, E. H., Piccardo, G., Vissers, R., & Rampone, E. (1991). Alpine olivine- and titanian clinohumite-bearing assemblages in the Erro-Tobbio peridotite (Voltri Massif, NW Italy). *Journal of Metamorphic Geology*, *9*(1), 79–91. <https://doi.org/10.1111/j.1525-1314.1991.tb00505.x>.
- Schmidt, M. W., & Poli, S. (1998). Experimentally based water budgets for dehydrating slabs and consequences for arc magma generation. *Earth and Planetary Science Letters*, *163*(1), 361–379. [https://doi.org/10.1016/S0012-821X\(98\)00142-3](https://doi.org/10.1016/S0012-821X(98)00142-3).
- Schmidt, M., & Poli, S. (2014). Devolatilization During Subduction. *Treatise on Geochemistry* (2nd ed., Vol. 4, pp. 567–591). <https://doi.org/10.1016/B978-0-08-095975-7-00321-1>.
- Schwarzenbach, E. M., Caddick, M. J., Beard, J. S., & Bodnar, R. J. (2016). Serpentinization, element transfer, and the progressive development of zoning in veins: evidence from a partially serpentinitized harzburgite. *Contributions to Mineralogy and Petrology*, *171*(1), 5. <https://doi.org/10.1007/s00410-015-1219-3>.
- Seydoux, L., & Baumgartner, L. P. (2013). Interactions fluide-roche dans les ultramafiques de la zone de Zermatt-Saas Fee. [unpublished Master Thesis].
- Seyfried, W. E. J., & Dibble, W. (1984). Seawater-peridotite interaction at 300°C and 500 bars: implications for the origin of oceanic serpentinites. *Geochimica et Cosmochimica Acta*, *44*, 309–321. [https://doi.org/10.1016/0016-7037\(80\)90139-8](https://doi.org/10.1016/0016-7037(80)90139-8).
- Shen, T., Hermann, J., Zhang, L., Lü, Z., Padrón-Navarta, J. A., Xia, B., et al. (2015). UHP metamorphism documented in Ti-chondrodite- and Ti-clinohumite-bearing serpentinitized ultramafic rocks from Chinese southwestern Tianshan. *Journal of Petrology*, *56*(7), 1425–1458. <https://doi.org/10.1093/ptrology/egv042>.
- Shen, T., Hermann, J., Zhang, L., Padrón-Navarta, J. A., & Chen, J. (2014). FTIR spectroscopy of Ti-chondrodite, Ti-clinohumite, and olivine in deeply subducted serpentinites and implications for the deep water cycle. *Contributions to Mineralogy and Petrology*, *167*(4), 1–15. <https://doi.org/10.1007/s00410-014-0992-8>.
- Sippl, C., Schurr, B., John, T., & Hainzl, S. (2019). Filling the gap in a double seismic zone: Intraslab seismicity in Northern Chile. *Lithos*, *346*, 105155. <https://doi.org/10.1016/j.lithos.2019.105155>.
- Skora, S., Mahlen, N., Johnson, C. M., Baumgartner, L. P., Lapen, T., Beard, B. L., et al. (2015). Evidence for protracted prograde metamorphism followed by rapid exhumation of the Zermatt-Saas Fee ophiolite. *Journal of Metamorphic Geology*, *33*(7), 711–734. <https://doi.org/10.1111/jmg.12148>.
- Spandler, C., Pettker, T., & Rubatto, D. (2011). Internal and external fluid sources for eclogite-facies veins in the Monviso meta-ophiolite, Western Alps: implications for fluid flow in subduction zones. *Journal of Petrology*, *52*(6), 1207–1236. <https://doi.org/10.1093/ptrology/egr025>.
- Spandler, C., & Pirard, C. (2013). Element recycling from subducting slabs to arc crust: A review. *Lithos*, *170*, 208–223. <https://doi.org/10.1016/j.lithos.2013.02.016>.
- Syracuse, E. M., van Keken, P. E., & Abers, G. A. (2010). The global range of subduction zone thermal models. *Physics of the Earth and Planetary Interiors*, *183*(1–2), 73–90. <https://doi.org/10.1016/j.pepi.2010.02.004>.
- Tenthorey, E., & Hermann, J. (2004). Composition of fluids during serpentinites breakdown in subduction zones: Evidence for limited boron mobility. *Geology*, *32*, 865–868. <https://doi.org/10.1130/G20610.1>.
- Thompson, G., & Melson, W. G. (1970). Boron contents of serpentinites and metabasalts in the oceanic crust: Implications for the boron cycle in the oceans. *Earth and Planetary Science Letters*, *8*, 61–65. [https://doi.org/10.1016/0012-821X\(70\)90100-7](https://doi.org/10.1016/0012-821X(70)90100-7).
- Trommsdorff, V., & Evans, B. W. (1972). Progressive metamorphism of antigorite schist in the Bergell tonalite aureole (Italy). *American Journal of Science*, *272*(5), 423–437. <https://doi.org/10.2475/ajs.272.5.423>.
- Trommsdorff, V., & Evans, B. W. (1974). Alpine metamorphism of peridotitic rocks. *Schweizerische Mineralogische und Petrographische Mitteilungen*, *54*, 333–354.
- Trommsdorff, V., Piccardo, G., & Montrasio, A. (1993). From magmatism through metamorphism to sea floor emplacement of subcontinental Adria lithosphere during pre-Alpine rifting (Malenco, Italy). *Schweizerische Mineralogische und Petrographische Mitteilungen*, *73*(2), 191–203.
- Trommsdorff, V., Sánchez-Vizcaino, V. L., Gomez-Pugnaire, M., & Müntener, O. (1998). High pressure breakdown of antigorite to spinifex-textured olivine and orthopyroxene, SE Spain. *Contributions to Mineralogy and Petrology*, *132*(2), 139–148. <https://doi.org/10.1007/s004100050412>.
- Ulmer, P., & Trommsdorff, V. (1995). Serpentine stability to mantle depths and subduction-related magmatism. *Science*, *268*(5212), 858–861. <https://doi.org/10.1126/science.268.5212.858>.
- van Keken, P. E., Hacker, B. R., Syracuse, E. M., & Abers, G. A. (2011). Subduction factory: 4. Depth-dependent flux of H<sub>2</sub>O from subducting slabs worldwide. *Journal of Geophysical Research*. <https://doi.org/10.1029/2010jB007922>.

- Vils, F. (2009). Boron, lithium and strontium isotopes as tracers of seawater-serpentinite interaction at Mid-Atlantic ridge, ODP Leg 209. *Earth and Planetary Science Letters*, 286(3–4), 414–425. <https://doi.org/10.1016/j.epsl.2009.07.005>.
- Vils, F., Müntener, O., Kalt, A., & Ludwig, T. (2011). Implications of the serpentine phase transition on the behaviour of beryllium and lithium–boron of subducted ultramafic rocks. *Geochimica et Cosmochimica Acta*, 75(5), 1249–1271. <https://doi.org/10.1016/j.gca.2010.12.007>.
- Vils, F., Pelletier, L., Kalt, A., Müntener, O., & Ludwig, T. (2008). The lithium, boron and beryllium content of serpentinized peridotites from ODP Leg 209 (Sites 1272A and 1274A): implications for lithium and boron budgets of oceanic lithosphere. *Geochimica et Cosmochimica Acta*, 72(22), 5475–5504. <https://doi.org/10.1016/j.gca.2008.08.005>.
- Weber, S., & Bucher, K. (2015). An eclogite-bearing continental tectonic slice in the Zermatt-Saas high-pressure ophiolites at Trockener Steg (Zermatt, Swiss Western Alps). *Lithos*, 232, 336–359. <https://doi.org/10.1016/j.lithos.2015.07.010>.
- Whitney, D. L., & Evans, B. W. (2010). Abbreviations for names of rock-forming minerals. *American Mineralogist*, 95(1), 185–187. <https://doi.org/10.2138/am.2010.3371>.
- Wicks, F., & Whittaker, E. (1977). Serpentine textures and serpentinization. *Canadian Mineralogist*, 15(4), 459–488.
- Wunder, B., & Schreyer, W. (1997). Antigorite: High-pressure stability in the system MgO·SiO<sub>2</sub>·H<sub>2</sub>O (MSH). *Lithos*, 41(1–3), 213–227. [https://doi.org/10.1016/S0024-4937\(97\)82013-0](https://doi.org/10.1016/S0024-4937(97)82013-0).
- Zanoni, D., Rebay, G., & Spalla, M. (2016). Ocean floor and subduction record in the Zermatt-Saas rodingites, Valtournanche, Western Alps. *Journal of Metamorphic Geology*, 34(9), 941–961. <https://doi.org/10.1111/jmg.12215>.

### Publisher's Note

Springer Nature remains neutral with regard to jurisdictional claims in published maps and institutional affiliations.

Submit your manuscript to a SpringerOpen<sup>®</sup> journal and benefit from:

- Convenient online submission
- Rigorous peer review
- Open access: articles freely available online
- High visibility within the field
- Retaining the copyright to your article

---

Submit your next manuscript at ► [springeropen.com](https://www.springeropen.com)

---